

A dynamics-based density profile for dark haloes – III. Parameter space

Benedikt Diemer^{*}

Department of Astronomy, University of Maryland, College Park, MD 20742, USA

ABSTRACT

In the previous paper of this series, we proposed a new function to fit halo density profiles out to large radii. This truncated Einasto profile models the inner, orbiting matter as $\rho_{\text{orb}} \propto \exp \left[-2/\alpha (r/r_s)^\alpha - 1/\beta (r/r_t)^\beta \right]$ and the outer, infalling term as a power-law overdensity. In this paper, we analyse the resulting parameter space of scale radius r_s , truncation radius r_t , steepening α , truncation sharpness β , infalling normalisation δ_1 , and infalling slope s . We show that these parameters are non-degenerate in averaged profiles, and that fits to the total profiles generally recover the underlying properties of the orbiting and infalling terms. We study the connection between profile parameters and halo properties such as mass (or peak height) and accretion rate. We find that the commonly cited dependence of α on peak height is an artefact of fitting Einasto profiles to the actual, truncated profiles. In our fits, α is independent of mass but dependent on accretion rate. When fitting individual halo profiles, the parameters exhibit significant scatter but otherwise follow the same trends. We confirm that the entire profiles are sensitive to the accretion history of haloes, and that the two radial scales r_s and r_t particularly respond to the formation time and recent accretion rate. As a result, r_t is a more accurate measure of the accretion rate than the commonly used radius where the density slope is steepest.

Key words: methods: numerical – dark matter – large-scale structure of Universe

1 INTRODUCTION

Fitting functions serve a two-fold purpose in astronomy: they provide simplified mathematical descriptions of complex objects or data, and they provide parameter spaces in which we can compare different observations, simulations, and theoretical models. One example is the density structure of dark matter haloes, which takes on enormously complex shapes in detail due to the irregular nature of the cosmic web and due to sub-structure. However, the spherically averaged density profiles of haloes are surprisingly well described by simple formulae such as that of Navarro, Frenk & White (1995, 1996, 1997, hereafter NFW), which models profiles as a two-parameter family of mass, M , and concentration, $c \equiv R/r_s$. Here, r_s is a scale radius and R denotes some definition of the outer radius (and thus mass) of the halo. A similar parametrisation of a normalization and r_s had been used before, but mostly in the context of describing galaxies (Jaffe 1983; Hernquist 1990; Dehnen 1993; Burkert 1995). Critically, NFW showed that concentration is essentially set by the formation epoch of a halo.

The mass-concentration parameter space has since been the basis of countless investigations, both theoretical (e.g., Bullock et al. 2001; Wechsler et al. 2002) and observational (e.g., Ettori et al. 2010). While the results have thus far confirmed our basic picture of halo structure (Umetsu 2020), there are also tales of caution. For example, galaxy cluster concentrations measured via weak lensing were persistently higher than expected from simulations, the so-called ‘over-concentration’ problem (e.g., Oguri et al. 2012; Wiesner

et al. 2012). This discrepancy turned out to be due to a correlation in the inferred masses and concentrations (Auger et al. 2013), showcasing the dangers of degenerate parameter spaces.

Moreover, on closer inspection, the M - c space turned out not to be quite sufficient to describe halo profiles accurately. The Einasto (1965, 1969) profile adds a third ‘steepening’ parameter α , which describes the rate at which the profile gradually steepens its logarithmic slope. This form describes halos more accurately (e.g., Merritt et al. 2006), even if it is reduced to a two-parameter function by setting the value of α to a constant (Wang et al. 2020a) or calibrating it as a function of peak height (Gao et al. 2008; Klypin et al. 2016). The chosen parametrisation matters because Einasto concentrations differ from NFW concentrations (Dutton & Macciò 2014) and because α and r_s can be degenerate in poorly constrained fits (Udrescu et al. 2019; Eckert et al. 2022).

Once we push beyond the virial radius, even three parameters are insufficient to describe the profiles in detail because they transition from being dominated by particles orbiting in the halo to being dominated by those falling in for the first time (e.g., Diemand & Kuhlen 2008, see, however, Lucie-Smith et al. 2022). This infalling term has a much shallower slope, predicted to be roughly $r^{-3/2}$ as long as shells of dark matter do not cross (Bertschinger 1985, see also Hayashi & White 2008). Even accounting for the resulting break, simulated profiles become steeper than the NFW or Einasto models near the transition, which led Baltz, Marshall & Oguri (2009) to multiply the NFW profile by a cutoff term that depends on a truncation radius, r_t , and a power-law exponent.

The steepening has since turned out to be a generic consequence of particle dynamics, namely, a manifestation of the limit of the phase-space distribution of orbiting particles. The position

^{*} Email: diemer@umd.edu

of this ‘splashback radius’ depends mostly on the mass accretion rate (Diemer & Kravtsov 2014, hereafter **DK14**; Adhikari, Dalal & Chamberlain 2014; More, Diemer & Kravtsov 2015). **DK14** proposed to model the splashback feature by multiplying the Einasto profile by a three-parameter truncation term, $[1 + (r/r_t)^\beta]^{-\gamma/\beta}$. The new parameters can be fixed or calibrated as a function of the accretion rate, leaving only the three original Einasto parameters. Nonetheless, the **DK14** parameter space suffers from a number of issues. First, β and γ lack a clear physical meaning because the asymptotic slope of the orbiting profile depends on r_s , r_t , α , and γ in a complex fashion. Second, when all parameters are left free, there are significant degeneracies that allow for unphysical parameter values despite reasonable profile shapes (Umetsu & Diemer 2017). This issue becomes particularly relevant when the **DK14** profile is used to infer properties of observed profiles, such as the extrapolated shape of the orbiting term (More et al. 2016; Baxter et al. 2017; Chang et al. 2018; Shin et al. 2019, 2021).

In this series of papers, we seek to build a better model by understanding the true shape of the orbiting term in and beyond the transition region. In Diemer (2022, hereafter Paper I), we presented a numerical algorithm that distinguishes orbiting and infalling simulation particles according to whether or not they have undergone at least one pericentre. We found that the orbiting term approaches arbitrarily steep slopes at its truncation, and that the profile shapes are affected by accretion rate, mass, and the slope of the linear power spectrum. In Diemer (2023, hereafter Paper II), we showed that the orbiting profiles are well-described by the form $\rho_{\text{orb}} \propto \exp[-2/\alpha (r/r_s)^\alpha - 1/\beta (r/r_t)^\beta]$, i.e., an Einasto profile that is exponentially cut off near the truncation radius (in addition to a power-law infalling profile). One of the main goals was to create a simpler, more meaningful parameter space that directly connects to the physical properties of halos and that has as few degeneracies as possible.

In this paper, we explore this new parameter space by charting the inter-relationships between best-fit parameters, as well as their relationships to mass, accretion rate, and formation time. As in Paper II, we analyse both individual profiles and averages over halo samples selected by mass and accretion rate. The paper is structured as follows. In Section 2, we briefly describe the underlying simulations, algorithms, halo selection, and fitting functions, but we refer the reader to Papers I and II for details. In Sections 3 and 4 we present our main results for averaged and individual halos, respectively. We further discuss these results in Section 5 and summarize them in Section 6. Supplementary figures are provided online on the author’s website at benediktdiemer.com/data. Throughout the paper, we follow the notation of Papers I and II.

2 SIMULATIONS AND METHODS

In this section, we briefly review our simulations and algorithms (Section 2.1), the selection of halos and the corresponding notation (Section 2.2), our new fitting function (Section 2.3), and how the best-fit parameters are calculated (Section 2.4). We refer the reader to Paper I for details on the simulations, algorithms, and halo definitions, and to Paper II for details on the new functions and fit quality.

2.1 N-body Simulations and algorithms

We base our analysis on the Erebus suite of N -body simulations (Diemer & Kravtsov 2014, 2015), which comprises 14 simulations of 1024^3 dark matter particles each. The suite covers different box

sizes as well as two Λ CDM cosmologies and four self-similar universes. The first Λ CDM cosmology is that of the Bolshoi simulation (Klypin, Trujillo-Gomez & Primack 2011), consistent with *WMAP7* (Komatsu et al. 2011), namely a flat Λ CDM cosmology with $\Omega_m = 0.27$, $\Omega_b = 0.0469$, $h = 0.7$, $\sigma_8 = 0.82$, and $n_s = 0.95$. The second is a Planck-like cosmology (Planck Collaboration et al. 2014, $\Omega_m = 0.32$, $\Omega_b = 0.0491$, $h = 0.67$, $\sigma_8 = 0.834$, and $n_s = 0.9624$). The initial power spectra for the respective simulations were generated using CAMB (Lewis, Challinor & Lasenby 2000). In contrast, the four self-similar Einstein-de Sitter universes have power-law initial spectra of slopes -1 , -1.5 , -2 , and -2.5 . These simulations allow us to isolate the impact of the initial power spectrum on the profile parameters (e.g., Knollmann, Power & Knebe 2008; Diemer & Kravtsov 2015; Ludlow & Angulo 2017).

We translate the power spectra into initial conditions using 2LP-Tic (Crocce, Puelblas & Scoccimarro 2006), and we evolve the particle distribution with GADGET2 (Springel 2005). We use the phase-space halo finder ROCKSTAR (Behroozi, Wechsler & Wu 2013) to identify haloes and subhaloes, which we connect across cosmic time using the CONSISTENT-TREES code (Behroozi et al. 2013). The resulting halo catalogues are described in detail in Diemer (2020).

The novel feature of our analysis is to split the halo density profiles into orbiting and infalling components with the algorithm presented in Paper I. Using the SPARTA framework (Diemer 2017, 2020), we follow the trajectories of each particle in each halo and determine its first pericentre, after which we classify the particle as orbiting rather than infalling (for alternative algorithms, see Sugiura et al. 2020; García et al. 2023; Salazar et al. 2024; Enomoto, Nishimichi & Taruya 2024). We have thoroughly tested the convergence and robustness of this algorithm in Paper I, and we refer the reader to that work for details.

2.2 Halo properties and selection

Wherever possible, we express density profiles in dimensionless units to scale out the absolute size and mass of halos. For this purpose, we normalize the density by the mean matter density of the universe, $\rho_m(z)$. The radial dimension can be rescaled by any halo radius R that can be reliably computed for each halo. We use the spherical overdensity radius R_{200m} , which is defined to enclose an average density of $200\rho_m(z)$. The corresponding enclosed mass is M_{200m} , which includes both bound and unbound particles. However, M_{200m} exhibits well-known dependencies on redshift and cosmology. We thus express mass as peak height, $\nu \equiv \nu_{200m} = \delta_c / (\sigma(M_{200m}))$, where $\delta_c = 1.686$ is the critical density for collapse (Gunn & Gott 1972) and σ is the variance of the linear power spectrum. This variance is measured on a scale of the Lagrangian radius of a halo, R_L , the comoving radius that encloses the halo mass at the mean density of the Universe, $M_{200m} = (4\pi/3)\rho_m(z=0)R_L^3$ (see Paper I). Another variable that has been shown to affect the structure of halos is the logarithmic slope of $\sigma(M)$,

$$n_{\text{eff}}(\nu, z) = -2 \left. \frac{d \ln \sigma(R, z)}{d \ln R} \right|_{R=R_L} - 3, \quad (1)$$

which is equivalent to $d \ln(P)/d \ln(k)$ for scale-free cosmologies with $P \propto k^n$. Thus, n_{eff} represents an effective slope of the power spectrum near the scales relevant for the formation of a halo (its Lagrangian radius). Finally, we define a dimensionless mass accretion rate $\Gamma \equiv \Gamma_{\text{dyn}} \equiv \Delta \ln M_{200m} / \Delta \ln a$, where Δa is one dynamical time defined as the time it takes to cross $2 R_{200m}$ (Paper I and Diemer 2020). The accretion over this timescale has been shown to corre-

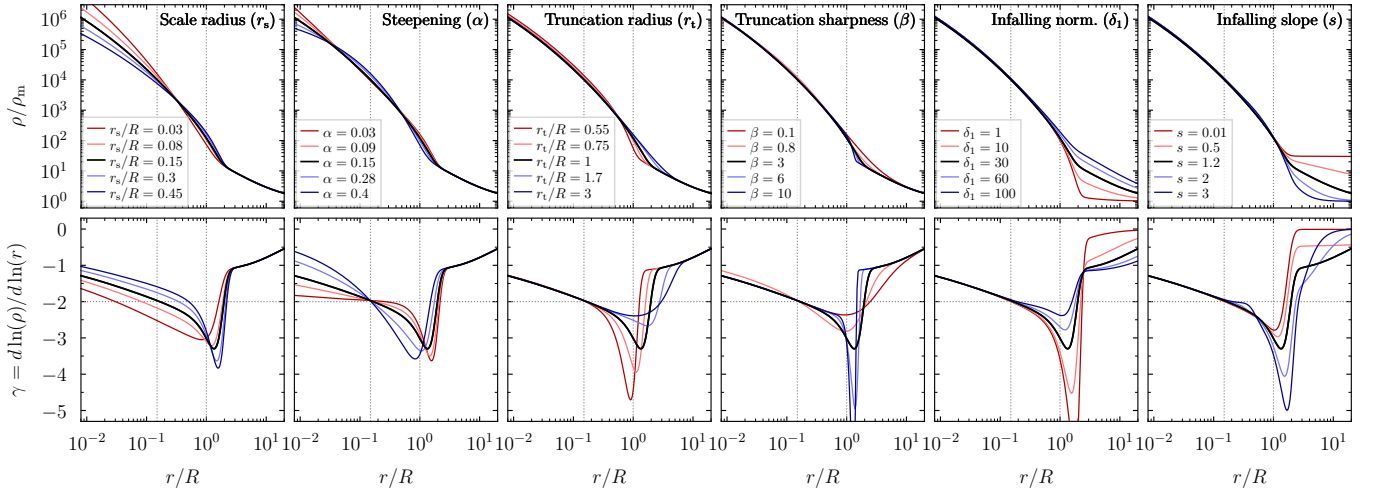


Figure 1. Impact of the parameters on our fitting function (Model B plus infalling profile). The reference profile (black line) is kept identical in each panel. We vary one parameter at a time within the ranges of values that we allow in our fits. We omit the fixed parameter η as well as δ_{\max} , which has no visible influence on the total profile. The normalisation of the orbiting profile, ρ_s , is adjusted such that all profiles enclose the same mass within R . The dotted vertical lines highlight the positions of the reference r_s and r_t .

late most tightly with halo structure, namely, with the position of the splashback radius (Shin & Diemer 2023).

We consider only host (isolated) halos that are resolved with at least 500 particles within R_{200m} , and we avoid halos that are experiencing strong interactions with a neighbour by limiting the fraction of unbound mass, $M_{200m, \text{all}}/M_{200m, \text{bnd}} < 1.5$. We measure the radial density profiles between 0.01 and $10 R_{200m}$, but we ignore the inner parts that are affected by the force resolution of the simulation or two-body scattering (Appendix A1 of Paper I; Ludlow, Schaye & Bower 2019; Mansfield & Avestruz 2021; Muni et al. 2024).

As in Paper II, we fit the density profiles of both individual halos and the average profiles of binned halo samples with certain properties, namely peak height ν , redshift z , and optionally accretion rate Γ . These samples contain halos from all Erebus simulation boxes that have sufficient resolution. In the self-similar universes, there is no physical time so that all redshifts are combined into samples with particular ν and Γ . Whenever we plot best-fit parameters as a function of the properties of halo samples, we refer to the median ν and Γ of the halos in a given sample. The effective power spectrum slope corresponding to a halo sample is computed from its median ν using equation (1).

2.3 Fitting function and parameters

Following the insight that the density profile is composed of orbiting and infalling particles with entirely different dynamics, we wrote $\rho(r) = \rho_{\text{orb}}(r) + \rho_{\text{inf}}(r)$ and suggested new forms for both terms in Paper II. We built upon the Einasto profile, where the shape of the orbiting term is determined by a normalization ρ_s and a radial evolution $S(r)$,

$$\rho_{\text{orb}}(r) = \rho_s e^{S(r)}. \quad (2)$$

The Einasto profile sets S such that the logarithmic slope becomes $\gamma \equiv d \ln \rho / d \ln r = -2(r/r_s)^\alpha$, i.e., a profile that gradually steepens at a rate α and reaches a slope of -2 at the scale radius r_s . We extend the Einasto form by a truncation term,

$$S(r) = -\frac{2}{\alpha} \left[\left(\frac{r}{r_s} \right)^\alpha - 1 \right] - \frac{1}{\beta} \left[\left(\frac{r}{r_t} \right)^\beta - \left(\frac{r_s}{r_t} \right)^\beta \right]. \quad (3)$$

This profile, which we called Model A, has a logarithmic slope of

$$\gamma(r) = -2 \left(\frac{r}{r_s} \right)^\alpha - \left(\frac{r}{r_t} \right)^\beta, \quad (4)$$

where the truncation radius r_t sets the location of the edge of the orbiting distribution and β determines how sharply the profile truncates. We also presented a slightly more complicated Model B, which gives almost identical profiles but reinstates the meaning of the scale radius as $\gamma(r_s) = -2$,

$$S = -\frac{2}{\alpha} \left[\left(\frac{r}{r_s} \right)^\alpha - 1 \right] - \frac{1}{\beta} \left[\left(\frac{r}{r_t} \right)^\beta - \left(\frac{r_s}{r_t} \right)^\beta \right] + \frac{1}{\eta} \left(\frac{r_s}{r_t} \right)^\beta \left[\left(\frac{r}{r_s} \right)^\eta - 1 \right], \quad (5)$$

where we set the nuisance parameter $\eta = 0.1$ throughout. As shown in Paper II, Models A and B are indistinguishable across almost all of parameter space, except where r_s approaches r_t . In this particular situation, Model B avoids a degeneracy between r_s and other parameters. We thus present Model B results throughout this paper, but we emphasize that the results for Model A are virtually identical (see online figures).

One of the insights of Paper I was that the infalling profile asymptotes to a fixed density at the halo centre. In Paper II, we found that the infalling term is thus well-described by a power law in overdensity with a normalization δ_1 , a slope s , and a maximum overdensity δ_{\max} ,

$$\rho(r) = \rho_m \left(\frac{\delta_1}{\sqrt{(\delta_1/\delta_{\max})^2 + (r/R)^{2s}}} + 1 \right). \quad (6)$$

In this paper, we mostly focus on fits to the total (orbiting plus infalling) profiles. Fig. 1 demonstrates that the interplay between these two components can significantly change the effect a parameter has on the overall profile shape. For example, even if we keep β constant, changing r_t produces a cutoff of a different sharpness because the truncation happens on top of a different density of infalling material; the same effect can be observed when changing δ_1 . All parameters change the shape of the truncation (or splashback) feature to some extent. We omit δ_{\max} from Fig. 1 since it does not appreciably affect the total profiles.

Fig. 2 shows examples of best-fit profiles to median profiles of

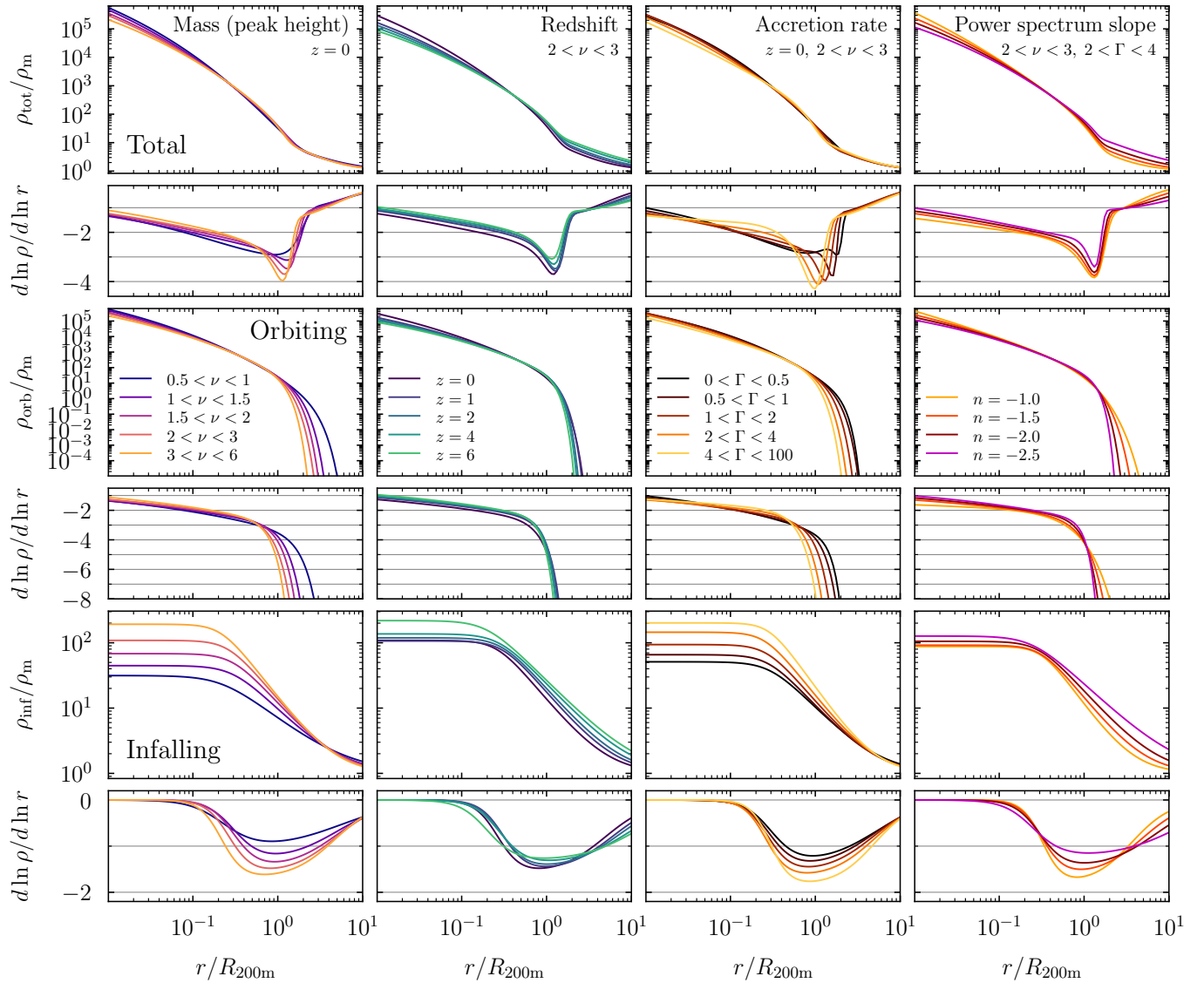


Figure 2. Dependence of the best-fit profiles on mass, redshift, accretion rate, and power spectrum slope (from left to right). The large panels show the median total, orbiting, and infalling profiles (from top to bottom), and the smaller bottom panels show the logarithmic slope. Many of the fits shown are also displayed in Paper II, but here we omit the simulation data to avoid crowding the figure. The profiles are selected to highlight trends in the best-fit parameters. Most notably, changing peak height causes a trend in the scale radius (the concentration-mass relation), and also a trend in the truncation radius. The latter, however, is almost purely driven by the accretion rate, which is responsible for large changes in r_t at fixed ν (third column). The accretion rate also changes α and the slope of the infalling term, s . Redshift barely influences the orbiting term but seems to alter the normalisation of the infalling term, δ_1 (second column). Physically, this effect is not due to cosmic time but due to changes in the effective slope of the power spectrum, n_{eff} . Even at fixed ν and Γ , n_{eff} further influences the profiles, as evidenced by the self-similar simulations with different n (right column). Here, higher n leads to power-law like profiles with low steepening α , as well as different infalling profiles.

halo samples with different masses (peak heights), redshifts, accretion rates, and power spectrum slopes. Paper I showed that the variations in mass and redshift are manifestations of underlying variations with accretion rate and power spectrum slope. The top, middle, and bottom sets of panels show the total, orbiting, and infalling profiles, respectively, highlighting the interplay between these components.

Recently, Salazar et al. (2024) introduced an alternative parametrisation for both the orbiting and infalling profiles. Their functions are designed to fit halo samples selected by orbiting mass (rather than $M_{200\text{m}}$, see also García et al. 2023). Nonetheless, both their form and equation 5 fit the orbiting profiles probed by their simulation well, although the two functions predict very different slopes

at $r \ll r_s$ (which could not be tested numerically). The Salazar et al. (2024) function replaces r_s with a varying slope, leaving a single radial scale akin to r_t . Their best-fit parameters are thus not directly comparable to this work. Salazar et al. (2024) also point out that the power-law infalling profile (equation 6) is designed to fit the overdensity ρ_{inf}/ρ_m within $r \lesssim 10 R_{200\text{m}}$. However, it fails at larger radii, especially when comparing the predicted correlation function, $\xi(r) \propto \rho_{\text{inf}}/\rho_m - 1$, to simulation data. Matching the correlation function out to large, linear scales demands a much more complex model, as shown by Salazar et al. (2024). We thus caution that equation 6 is a purely phenomenological fitting function that should not be extrapolated beyond $10 R_{200\text{m}}$.

2.4 Fitting method

Our fitting routine is described in detail in Paper II, but we briefly summarise it for completeness. We use a least-squares fit to minimise the Cauchy loss function of the logarithmic difference between simulated and fitted profiles,

$$\chi_{\text{cauchy}}^2 \equiv \sum_i \ln(1 + \chi_i^2) \quad \text{with} \quad \chi_i \equiv \frac{\ln \rho_{i,\text{fit}} - \ln \rho_{i,\text{data}}}{\ln(1 + \sigma_i/\rho_{i,\text{data}})}, \quad (7)$$

where i indexes the radial bins and σ_i is the uncertainty in $\rho_{i,\text{data}}$. The Cauchy function reduces the influence of outliers in the fit, which leads to more physically meaningful best-fit parameters. For averaged profiles, σ_i is the sum of a bootstrap estimate of the statistical uncertainty and a 5% systematic error that is added in quadrature in order to avoid low- σ bins dominating the fit. For individual halos, the bootstrap estimate is replaced by a Poisson-like statistical uncertainty.

All parameters are translated to log space for fitting. We estimate their uncertainty from the covariance matrix $\mathbf{C} = (\mathbf{J}^T \mathbf{J})^{-1}$, which is in turn computed from the Jacobian matrix returned by the fitting routine. However, the Jacobian refers to changes in the χ^2 measure, whose normalization directly depends on unreliable assumptions about the uncertainties in the profiles (such as the systematic error discussed above). We thus renormalize the covariance matrix and compute the parameter uncertainties from its diagonal,

$$\sigma_{p,j} = \sqrt{\mathbf{C}_{jj} \times \chi^2/N_{\text{dof}}}, \quad (8)$$

where the index j runs over the number of parameters. This renormalization assumes that the ‘true’ $\chi^2/N_{\text{dof}} \approx 1$, i.e., that the fit is reasonably good and that a large or small χ^2/N_{dof} must be caused by over- or underestimated errors. Moreover, our expression for $\sigma_{p,j}$ ignores degeneracies between the parameters and should thus be seen as a rough estimate. We show the uncertainties on parameters as gray error bars in the following figures. Routines for fitting the new profile are implemented in the public python package *Colossus* (Diemer 2018).

3 PARAMETERS FROM AVERAGED PROFILES

In this section, we investigate the best-fit parameters from fits to the mean and median profiles of various halo samples. Our goal is to establish whether the fitting function presented in Section 2.3 produces a non-degenerate, physically meaningful parameter space. We investigate the distribution of parameters and potential degeneracies in Section 3.1. In Section 3.2, we connect the parameters to the physical properties of halos such as mass, accretion rate, redshift, and cosmology. We mostly focus on fits to the total profiles rather than separate fits to the orbiting and infalling terms. While the parameters from the latter are closer to the ‘true’ underlying shapes of the two terms, we only have access to the total profiles in typical applications — most notably, in observational data. However, in Section 3.3 we show that the total fits generally recover the parameters from the separate fits well. We use model B throughout, but we emphasize that model A gives identical best-fit parameters in the vast majority of cases (Paper II).

Fig. 2 shows a selection of fits arranged to highlight the dependence of the profiles on halo mass, accretion rate, redshift, and the slope of the power spectrum. This figure will serve as a visual guide while we discuss the respective trends from the perspective of the best-fit parameters.

3.1 Parameter relations and degeneracies

Fig. 3 shows the best-fit parameters from fits to all mass-selected samples, as long as their average profiles are based on at least 80 profiles (Paper II). We remove two samples where the fit did not result in converged parameters (low ν bins in the $n = -1$ cosmology and in WMAP7 at $z = 4$). Each fit is shown as a set of points with a certain color (peak height) and shape (redshift and cosmology). The uncertainties are shown as gray error bars (Section 2.4).

The figure is segmented into three areas: the bottom-left triangle (lightly shaded blue) shows the results from fits to median profiles, the top-right triangle (light yellow) those from mean profiles, and the diagonal (gray shaded) panels compare the results from mean and median fits for each parameter. These comparisons are important because the median profiles are less susceptible to outliers and often lead to more well-defined trends in the best-fit parameters, but stacked observations correspond to mean profiles. The mean profiles prefer a systematically slightly lower truncation radius and a higher normalization of the infalling profile, δ_1 , presumably owing to nearby neighbours that can strongly up-scatter the amplitude of the infalling profile. Other than that, the mean and median parameters generally agree well.

Overall, the parameters occupy a large fraction of the allowed space. We immediately notice some correlations between parameters, but those do not necessarily indicate degeneracies in the fit.¹ Instead, many of them are characterized by a sequence in mass (colour), where both parameters change in unison as a function of mass. We note that r_s and α appear more or less uncorrelated, which is a relief given that they can be notoriously degenerate in under-constrained fits. Similarly, r_t and β are basically uncorrelated, which indicates that the profiles constrain their values beyond a generic steepening of the slope. Meanwhile, the two radial scales, r_s and r_t , are correlated with a clear trend in ν (colour), which we will explain by the correlation of each with accretion rate. The steepening parameters α and β are correlated but positively, which is not what we would expect if they were trading off each other to create profiles of a particular steepness. The normalisation of the infalling profile also falls on sequences in peak height, for example when plotted against the spatial scales r_s and r_t . The infalling slope, s , however, is more or less uncorrelated with the other parameters. The central infalling overdensity δ_{max} is omitted from the figure as it has no influence on the total profile.

We do not observe any strong trends with redshift, which would manifest as squares/triangles occupying different areas than circles ($z = 0$). This non-evolution agrees with our finding that the orbiting profiles are only weakly redshift-dependent (Fig. 2). There is a trend in the normalization of the infalling profile (δ_1), but it is hard to discern in Fig. 3. We also do not notice any obvious trends with cosmology (filled/open symbols). The self-similar cosmologies (crosses and pluses) tend to span a wider range than different Λ CDM redshifts, which makes sense given that the redshift evolution in Λ CDM cosmologies essentially represents an interpolation of the different

¹ We have omitted ρ_s from the figure, which at first sight appears to be highly degenerate with r_s . This degeneracy is a consequence of our parametrisation that uses ρ_s/ρ_m and $r_s/R_{200m} = 1/c_{200m}$. From integration, $\rho_s/\rho_m = 200 c_{200m}^3 / (3f[c_{200m}])$, where $f(r/r_s)$ is a dimensionless function of order unity (e.g., $f(x) = \ln(1+x) - x/(1+x)$ for an NFW profile). Any deviations from this relation indicate that the normalization of the fitted and simulated profiles differ slightly, or that there are slight deviations in $f(r/r_s)$ because our profile is also a function of r/r_t .

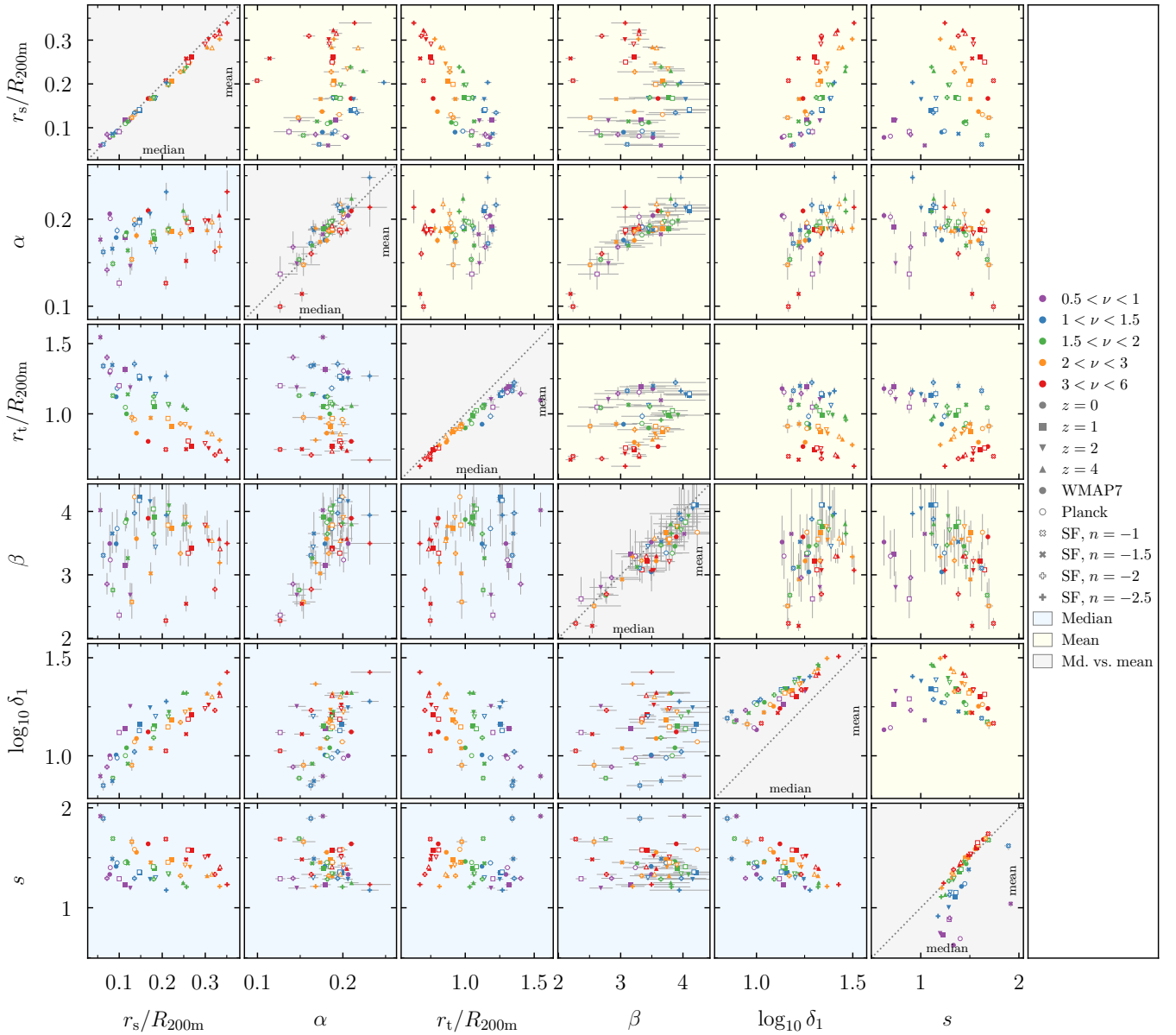


Figure 3. Best-fit parameters from fits to the total (orbiting plus infalling) profiles of all mass-selected samples. The bottom-left half (light-blue background) shows the fits to median profiles, and the right-top half (yellow background) mean profiles. The gray diagonal panels compare the median and mean parameters (with median on the x -axis). Colours indicate ν bins, and symbols redshifts as indicated in the legend. Filled symbols correspond to the WMAP7 cosmology, empty symbols to Planck. The self-similar cosmologies (where all redshifts are combined into a single sample) are shown as filled/empty crosses and pluses. Overall, the parameters from mean and median fits agree well. Wherever parameters fall on tight relations with each other, those sequences are explained by changes in peak height (colour), indicating that none of the profile parameters are strongly degenerate (see Section 3.1 for details).

power spectrum slopes probed by the self-similar universes (Paper I).

Some of the trends we have observed are readily explained by dependencies on the mass accretion rate, which has a stronger impact on the profiles than mass. Fig. 4 shows the same plot as Fig. 3, but for Γ -selected samples. The point colour now indicates Γ rather than ν . We have chosen the $2 < \nu < 3$ bin because the fit parameters are particularly well-determined for high-mass halos, but other ν bins lead to qualitatively similar conclusions (see online figures). The error bars tend to be larger than for ν -selected samples because the profiles exhibit a greater variety of shapes and are thus harder to fit (Paper II).

Overall, the median and mean fits agree excellently for Γ -selected profiles. We observe essentially no systematic differences in any of the parameters for the orbiting profile, and the infalling slopes s also agree in well-constrained profiles. As in Fig. 3, by far the largest differences occur in δ_1 , indicating that a few halos with high infalling profiles increase the mean compared to the median. The relationships between parameters are also clearer in Fig. 4. Most notably, the parameters that describe the steepening of the profile (α , β , and r_t) fall on tight relations that are clearly determined by the accretion rate (rather than by degenerate fits). The anti-correlation of r_s and r_t can easily be explained based on the general shape of formation histories. Concentration is tightly related to the ‘formation

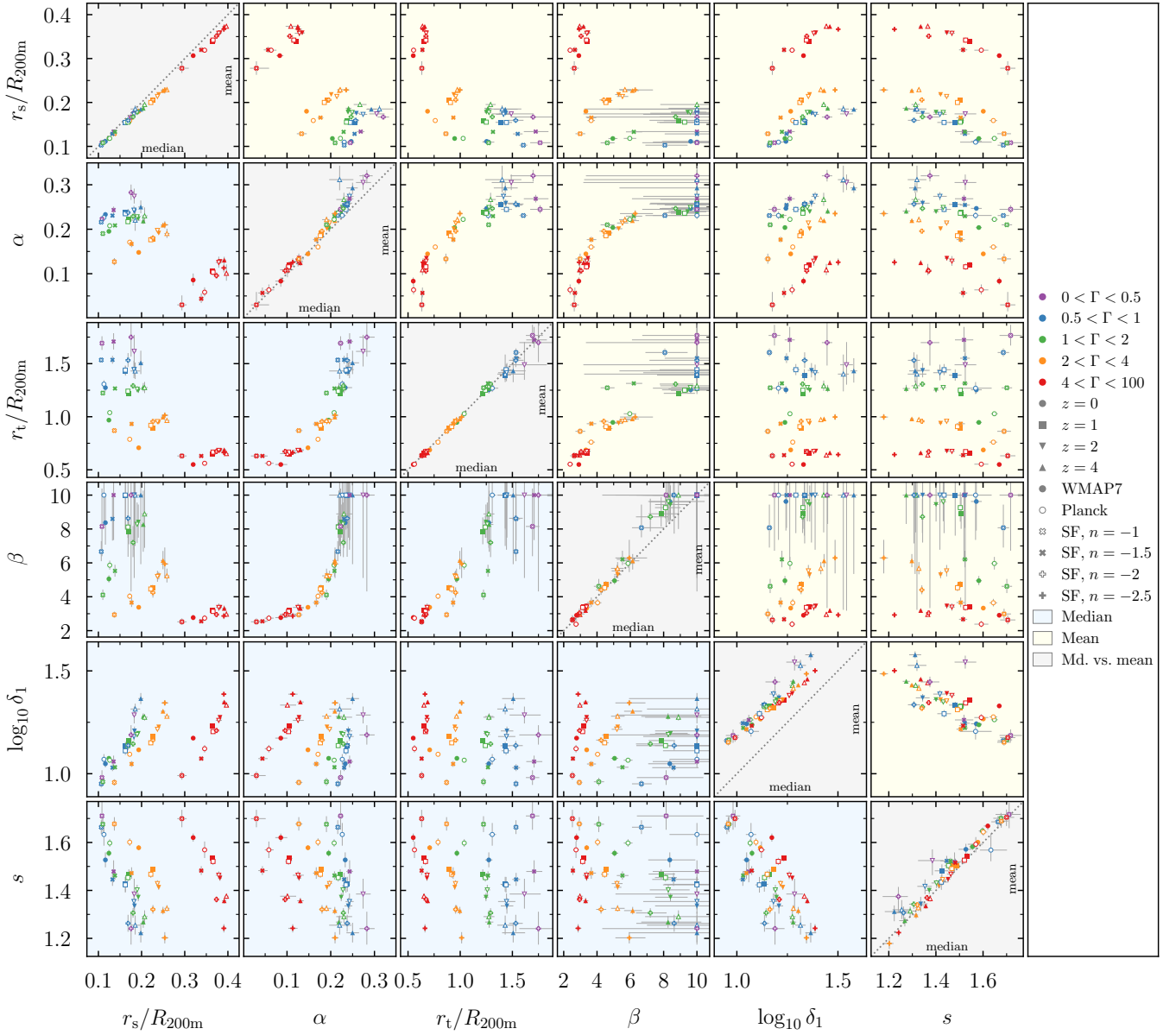


Figure 4. Same as Fig. 3, but for accretion rate-selected samples with $2 < \nu < 3$. The respective plots for the other ν bins appear generally similar, although there is more scatter at low and high ν . Many parameters exhibit strong trends with Γ (colour), most notably α , r_t , and β . As for the ν -selected samples, the mean and median parameters mostly agree, with the exception of the normalisation of the infalling profile, which is sensitive to nearby neighbours.

time’ when the halo transition from fast to slow accretion (Navarro, Frenk & White 1997; Wechsler et al. 2002; Tasitsiomi et al. 2004; Zhao et al. 2009; Ludlow et al. 2013), whereas r_t captures recent accretion (Shin & Diemer 2023). Specifically, a high accretion rate leads to added matter, contracting orbits, and thus a smaller r_t (or splashback radius, see Adhikari, Dalal & Chamberlain 2014). These qualitative results are also supported by AI-based decompositions of profiles that are entirely agnostic of any fitting functions (Lucie-Smith, Peiris & Pontzen 2024). Since halos that formed earlier tend to accrete slowly today, a higher concentration means a lower r_s and a higher r_t (and vice versa). However, the r_s - r_t relation maintains roughly the same amount of scatter as for ν -selected samples, highlighting the fundamental two-scale nature of the profiles that cannot

be captured by a single radius parameter (see Section 5.1 for further discussion).

The truncation tends to be sharper in Γ -selected samples, leading to much higher values of β (although some of the most extreme values are poorly constrained). Moreover, slowly accreting halos (with large r_t) exhibit particularly sharp cutoffs (large β). The infalling profiles are also strongly influenced by Γ (Fig. 2), but δ_1 and s exhibit significant scatter at fixed Γ due to their dependence on mass and cosmology.

3.2 Dependence on halo properties, redshift, and cosmology

To better understand how the physical conditions of halos translate into their density profiles, we now plot the best-fit parameters of the

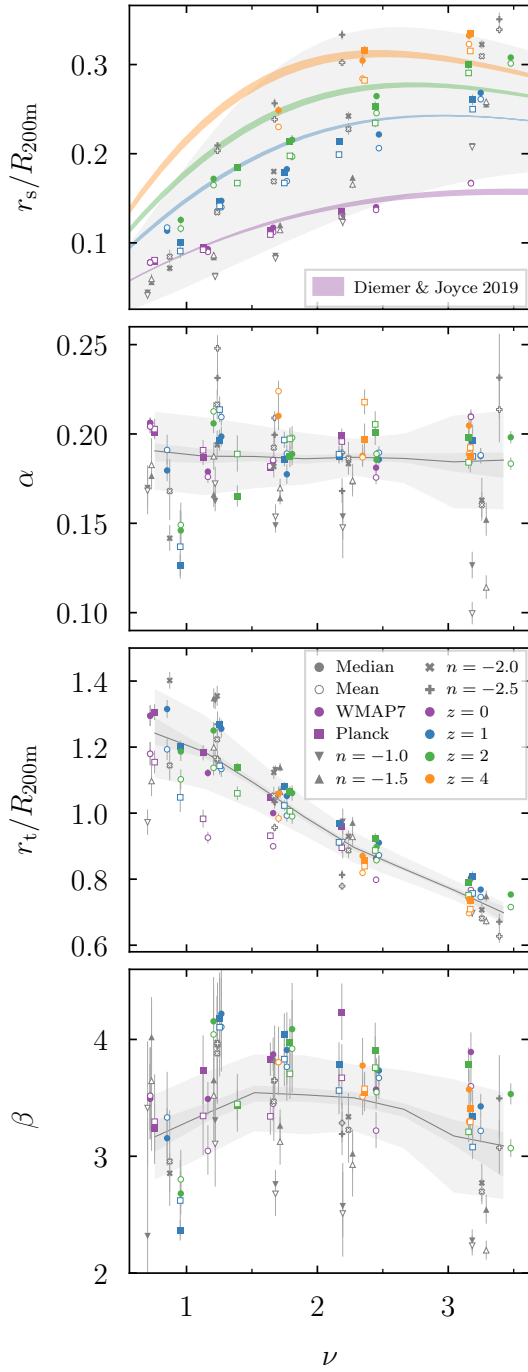


Figure 5. Dependencies of the best-fit parameters on peak height. Each point marks a fit to a total profile, with its shape indicating the cosmology, its colour the redshift (gray for self-similar cosmologies), and empty/full symbols indicating fits to mean/median profiles. The gray lines and contours show a kernel-smoothed running median and scatter. The trends can be roughly understood as follows. In the top panel, $r_s/R_{200m} = 1/c_{200m}$ increases with halo mass as expected. The fits roughly match the predictions of Diemer & Joyce (2019), although their model was calibrated on the NFW concentrations of individual halos. The shaded regions enclose the variations due to cosmology, which are large for the self-similar universes (gray area). The second panel demonstrates that our fits suggest a constant α - ν relation (see further discussion in Section 3.2.2). The third panel shows that r_t/R_{200m} (and thus the splashback radius) decreases with ν because the average mass accretion rate increases. Finally, we find no significant trend of β with ν .

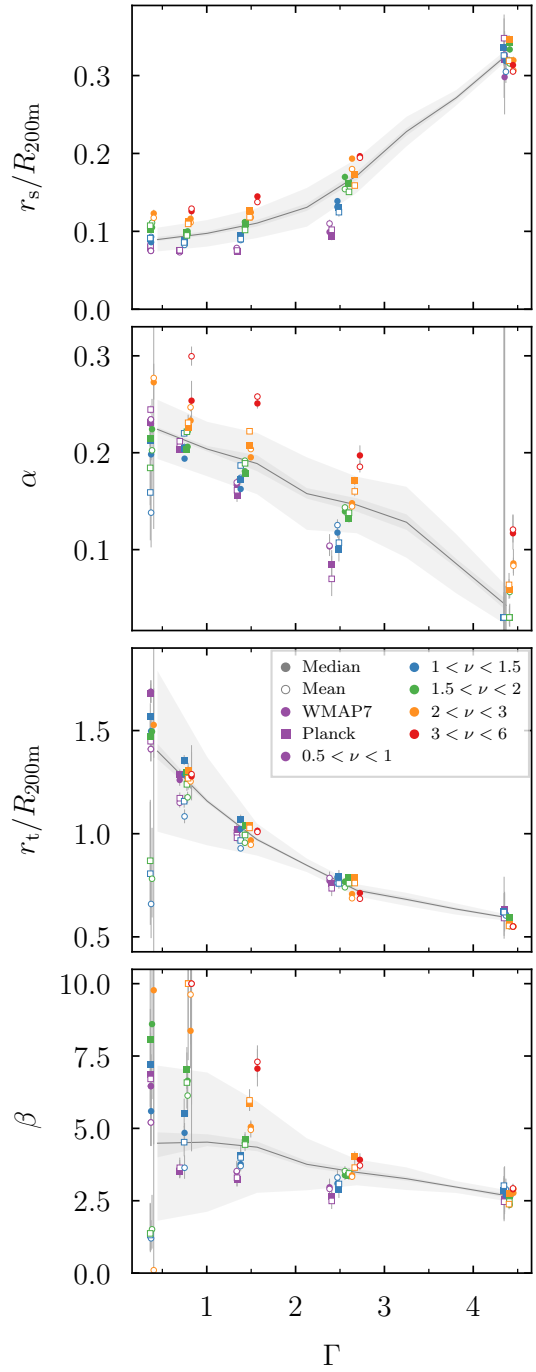


Figure 6. Same as Fig. 5 but for dependencies on the accretion rate Γ . The point colours now represent peak height. We omit higher redshifts and the self-similar simulations to avoid crowding, but our conclusions hold regardless. The top panel shows a clear relation between Γ and $r_s/R_{200m} = 1/c_{200m}$, which is physically expected since faster-accreting halos are younger and thus have lower concentration. However, the relation is complicated by secondary dependencies on ν and z . Second, α decreases towards high Γ to accommodate profiles that increasingly approach power laws (Paper I). The truncation radius (third panel) exhibits a well-defined relation with Γ . Finally, β weakly but noticeably decreases with increasing Γ . This trend may seem counter-intuitive given that the sharp cutoffs are easier to discern in fast-accreting halos, but it is congruent with the profiles shown in Fig. 2. The total profile is also modulated by the infalling term, which itself depends strongly on Γ (Fig. 8).

orbiting profile against halo mass (Fig. 5) and accretion rate (Fig. 6). The meaning of the symbols and colors has changed compared to Figs. 3 and 4: filled/open symbols now denote median/mean fits, shape denotes cosmology, and colour denotes redshift in Fig. 5 and peak height in Fig. 6. The latter shows results for $z = 0$, but the conclusions are qualitatively similar for other redshifts (although some of the relations evolve with z).

The gray lines and contours show a smoothed median, its uncertainty, and its scatter as computed by kernel-localized linear regression (KLLR, Farahi et al. 2018; Anbajagane, Evrard & Farahi 2022). We use a Gaussian filter with a width of 10% of the x -extent of the plotted points. The uncertainty on the points is taken into account when computing the median and scatter. We assign a minimum uncertainty of 1% of the y -extent of the points to avoid numerical issues. The calculation of the weighted scatter can fail, in which case we fall back to the unweighted scatter (which tends to be similar). We now discuss trends in each profile parameter in turn.

3.2.1 Concentration

The top panel of Fig. 5 shows the inverse of the concentration-mass relation, since $r_s/R_{200m} = 1/c_{200m}$. We omit the smoothed median from this panel because we expect a well-known redshift dependence of the concentration-peak height relation (Prada et al. 2012; Diemer & Kravtsov 2015). Instead, the shaded regions show the predictions of the Diemer & Joyce (2019) model for the c - ν relation at the four redshifts for which points are plotted. The width of the contours represents the differences between the WMAP7 and Planck cosmologies. The gray contour shows the range predicted for the self-similar cosmologies. We should not expect a perfect match to these predictions because the Diemer & Joyce (2019) model was calibrated to match the concentrations of individual halos rather than those of stacked profiles. Moreover, c was measured by fitting NFW rather than Einasto profiles, which leads to slightly different concentrations (Dutton & Macciò 2014, see further discussion in Section 5.2). Nonetheless, our profiles obey a comparable c - ν relation with a similar redshift trend. As expected from the large gray contour, the self-similar fits scatter across a wide region that mostly encloses the Λ CDM results. Fig. 6 reveals that concentration (or r_s/R_{200m}) does correlate significantly with accretion rate in the expected fashion, where young halos in the fast-accretion regime have low concentration (e.g., Wechsler et al. 2002; Zhao et al. 2009). Any residual correlation with ν manifests itself as a colour gradient in the points.

3.2.2 The steepening parameter α

In Fig. 7, we revisit the question of whether the steepening parameter α evolves with peak height. Conventional wisdom has it that α increases with ν , more or less independently of redshift and cosmology (Gao et al. 2008; Dutton & Macciò 2014; Klypin et al. 2016; Udrescu et al. 2019; Brown et al. 2022). The fitting functions of Gao et al. (2008) and Klypin et al. (2016) are shown as yellow and red areas, respectively. They take on a finite width because they were calibrated for ν_{200c} , whose conversion from the ν_{200m} on the x -axis depends slightly on redshift and cosmology. Nevertheless, these relations provide a clear prediction that α should change from ≈ 0.15 at low ν to ≈ 0.25 at high ν .

Surprisingly, we find no such trend at all! Instead, the fits scatter around a median value of $\alpha \approx 0.18$ at all peak heights. Fig. 2 confirms that there is no indication that the slope steepens more rapidly

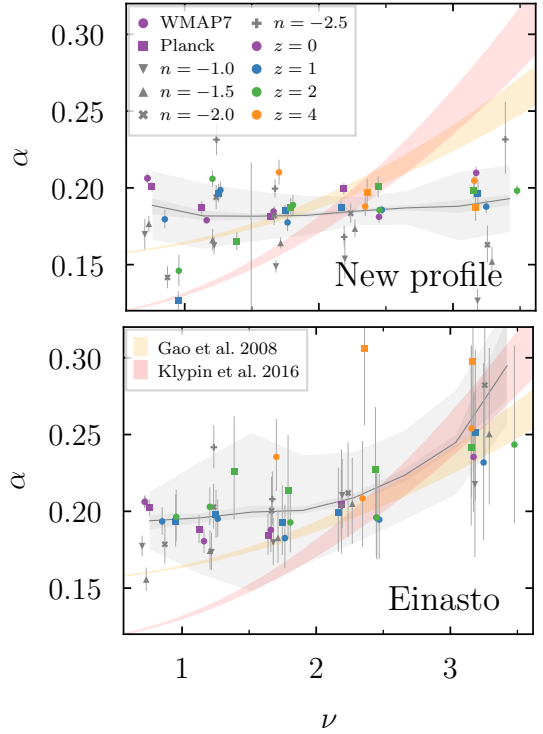


Figure 7. The dependence of the profile steepening parameter α on peak height when inferred via our new fitting function (top) or the conventional Einasto profile (bottom). Both forms are combined with a power-law infalling profile. We focus on fits to median profiles. As shown in Fig. 3, α shows no evolution with peak height in our new model, which is in tension with the increasing steepening suggested in the literature (Gao et al. 2008; Klypin et al. 2016, yellow and red shaded areas). We do, however, recover a similar relation when fitting the Einasto profile. The trend in α arises when fitting profiles that steepen more strongly than the Einasto function naturally predicts. As the profile truncation gets steeper at high ν (Fig. 2), the best-fit values of α increase to ameliorate a poor fit near the truncation. Since r_t and β capture the truncation in our new model, α is determined by the inner profiles ($r \ll r_t$), which prefer a roughly constant α .

at small radii for high- ν than for low- ν halos. However, when fitting the Einasto profile without the truncation term (bottom panel of Fig. 7), we qualitatively reproduce the rising α found by other works. This difference demonstrates that the conventional ν - α relation is an artefact of the Einasto profile not quite fitting the steepening slopes near the truncation. While the inner profiles prefer more or less constant values of α , higher- ν halos experience a truncation at smaller radii because of their smaller splashback radii (Fig. 2). Such profiles produce higher best-fit values of α because the fit tries to match the steepening at large radii. The resulting fits may still look acceptable, leading many authors to the conclusion that the Einasto profile produces universally good fits (e.g., Navarro et al. 2010; Wang et al. 2020a; Zhou & Han 2024). Moreover, the differences in α will depend on details of the fit such as the relative weighting of bins and the outermost radius.

Even though α does not evolve with ν when fitting our new model, it does decrease with accretion rate (second panel of Fig. 6). This trend arises because of the fairly flat, power-law like profiles of fast-accreting halos (Paper I and Fig. 2). When averaging over different accretion rates to create ν -selected bins, the trend appears to be washed out, leading to the constant α seen in Fig. 7.

Another result based on Einasto fits is that at fixed ν , α depends on the slope of the power spectrum, n_{eff} (Nipoti 2015; Ludlow &

Angulo 2017; Brown et al. 2020, 2022). Although not obvious from the profiles in the self-similar simulations (Fig. 8 in Paper I), this trend is visible in Fig. 7, where gray triangles ($n = -1$ and -1.5) fall below the median and crosses and pluses ($n = -2$ and -2.5) lie above it. The n_{eff} -dependence at fixed ν can be understood in more general terms, as shown by Brown et al. (2022). The shape of the density profiles, and thus parameters such as c and α , depend on the shape of the power spectrum over a wide range of scales. The filter used to compute peak height (e.g., a top-hat) reduces this dependence to a single number, but it does not optimally capture the scales that actually influence α , leading to a remaining dependence on the power spectrum that can be summarily parametrised with n_{eff} . A similar logic holds for concentration: we can either parametrise it as $c(\nu, n)$ (Diemer & Kravtsov 2015) or as a function of only an altered definition of ν (Brown et al. 2022).

3.2.3 The truncation radius and truncation sharpness

We now turn to the location and shape of the truncation. The third panel of Fig. 5 shows that our best-fit truncation radii decrease with ν , although with modest variations between $0.6 \lesssim r_t \lesssim 1.4$. The gray median line in Fig. 5 is well approximated as $r_t/R_{200m} \approx 1.4 - 0.21\nu$. This relation differs significantly from that of DK14 because r_t takes on a different meaning in their formula for ν -selected profiles (their equation 6). The trend with ν is almost entirely driven by changes in the average accretion rate, which leads to much stronger variations in r_t (third panel of Fig. 6). We defer a more detailed analysis of the relation between the truncation radius, accretion rate, and the splashback radius in Section 5.3.

Finally, β does not vary systematically with ν , which is congruent with the profiles shown in Fig. 2. The changes in profile shape are clearly driven by r_t , which does significantly decrease with ν . We do observe a slight decrease of β with Γ , but it is not clear how significant this trend is given the large scatter at low Γ . Moreover, Fig. 4 shows that β and α are highly correlated. These findings raise the question of whether β really describes a physical reality or whether it is a ‘nuisance’ parameter. We have experimented with fixing $\beta \sim 4$ and find acceptable fits to most total profiles. However, many of the stacked orbiting terms are fit significantly less well, especially for the mean profiles. While the scatter in the Γ - r_t relation is reduced, the median does not change significantly. Similarly, the parameters of the inner profile (r_s and α) do not qualitatively change. We thus conclude that β may not be directly connected to an obvious physical halo property, it does seem to capture a truncation shape that does genuinely vary between halo samples.

3.2.4 The infalling profile

Fig. 2 demonstrates that the infalling shapes vary systematically with Γ and n_{eff} , whereas much of the dependence on ν is due to the ν - Γ relation and nearby neighbours (Paper I). Fig. 8 shows the dependence of the infalling profile parameters on Γ . Here, we consider the results of a separate fit to the infalling profile only because the trends are somewhat less clear in the total fits, and because δ_{max} is kept fixed in the total fit.

Perhaps unsurprisingly, the normalization of the infalling profile is higher in fast-accreting halos. If material falls in with some characteristic velocity, a higher flow rate implies more infalling material (e.g., De Boni et al. 2016). Unlike the orbiting profile, the infalling profile is subject to a strong redshift trend: the median normalization δ_1 increases by about 60% between $z = 0$ and $z = 4$ (see also Fig. 6

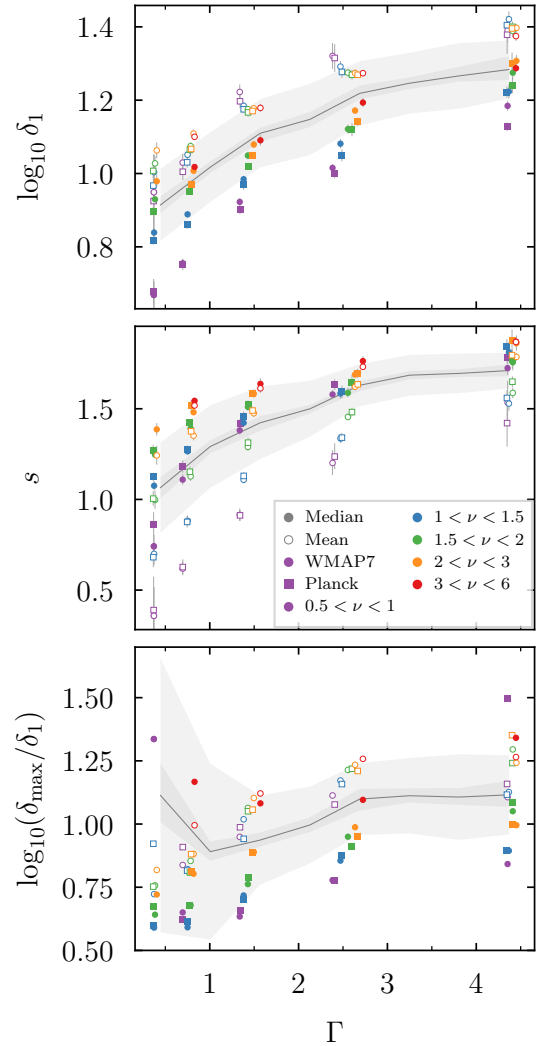


Figure 8. Same as Fig. 6 but for the infalling profile. We show parameters based on fits to only the separate infalling profiles because the relations are somewhat less clear when fitting the total profiles (see online figures). The infalling profiles of fast-accreting halos exhibit a higher normalization (top panel), a steeper slope (middle panel), and approach a higher asymptotic density at the halo centre (bottom panel, which shows the more or less constant ratio between δ_{max} and δ_1). All parameters show a clear dependence on whether we fit the median or mean profiles (filled or empty symbols), highlighting the asymmetric distribution of infall densities around the mean.

in Paper I), but this increase can be understood as an effect of n_{eff} rather than cosmic time (Paper I).

The slope s becomes steeper with Γ , approaching $s \approx 1.5$ at high accretion rates, which is the value predicted for non-crossing, collapsing shells (Bertschinger 1985, see DK14 for a similar result). This picture should break down around the splashback radius, which occurs at larger radii for low- Γ halos. Once the mass interior to infalling particles decreases as they move inwards, their density profile flattens (see discussion in Paper I). It is possible that this mechanism causes the decrease in s at low Γ , but we leave it to future work to understand the reasons in detail.

The asymptotic maximum density at the halo centre increases with Γ , but this trend is perhaps easier understood by considering the ratio $\delta_{\text{max}}/\delta_1$ as shown in the bottom panel of Fig. 8. The relatively constant ratio suggests that the infalling profile reaches a maximum

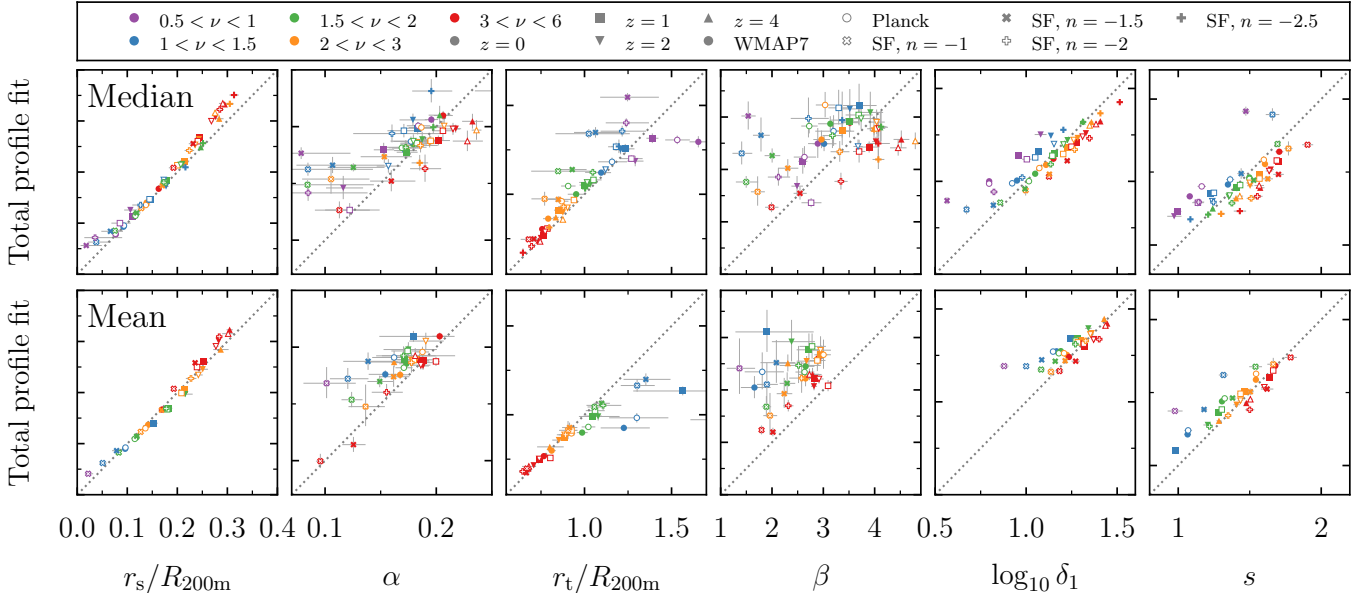


Figure 9. Recovery of best-fit parameters from separate fits to the orbiting and infalling terms (x-axis) by fits to the total profile (y-axis). The two rows show results from fits to the median (top) and mean (bottom) profiles of ν -selected samples. The symbols have the same meaning as in Fig. 3. The good agreement for r_s is expected because the inner region of halos is strongly dominated by the orbiting term, but the truncation radius r_t can be strikingly well recovered from total fits. The exception are low-mass haloes (purple/blue), which do not exhibit a strong steepening feature and are less relevant observationally. The agreement is less clear for the steepening parameters α and β , especially in the mean profiles. However, these parameters also carry somewhat less physical meaning and can be fixed. The parameters of the infalling profile are recovered reliably, especially in high-mass haloes. See Section 3.3 for details.

that is a fixed multiple, about ten times, its normalization at R_{200m} . This limit could be related to the typical fractions of radial and tangential particle orbits, but we defer a more detailed investigation to future work. Some outlier points correspond to fits where the central density is unconstrained and takes on its maximum value of $10^4 \rho_m$.

3.3 Recovering parameters from the total profile

Our insights into the separate orbiting and infalling profiles are only meaningful if they can be recovered by fits to the total profiles, which are available observationally and in unsplit simulation data. In this section, we investigate how accurately the two sets of parameters track each other, or, in other words, how much knowledge about the profiles is lost in the superposition of orbiting and infalling matter. Fig. 9 shows the relationship between the best-fit parameters from the separate orbiting/infalling fits (on the x-axis) and from the total fits (on the y-axis). We consider ν -selected samples, but the conclusions hold for Γ -selected samples. We omit ρ_s because the correspondence is very good as expected, as well as δ_{max} , which is not varied in the total fits. We consider both median profiles (top row) because they show the clearest trends in fit parameters and mean profiles (bottom row) because they correspond most closely to stacked observations. We do not find strong differences between median and mean profiles in Fig. 9.

Most importantly, the radial scales r_s and r_t are both recovered reliably. While the tight correlation between total and separate fits might be expected at small, orbiting-dominated radii such as r_s , it is a positive surprise for r_t , which measures the position of the transition region that is by construction most affected by the superposition of orbiting and infalling matter. At low mass (blue/purple points in Fig. 9), the correlation in r_t degrades, mostly because of erratic fits to separate profiles that contain significant contributions from

neighbours (Paper I). This issue is of little importance because observations will, for the foreseeable future, focus on group and cluster haloes.

Recovering the steepening parameters α and β is much harder, especially at low mass. Here, the infalling term conceals the sharpness of the truncation that is captured by β . Both parameters are biased high in the total fits and are subject to significant scatter. However, those parameters convey less physical meaning than r_s and r_t , and they can be set to fixed values or limited by an informative prior (Paper II). The parameters of the infalling profiles, δ_1 and s , are broadly recovered, especially at high ν .

In summary, the total profiles contain crucial information about the orbiting and infalling terms and the transition region. We note that the fitting procedure matters for these results. For example, by down-weighting outlier points, the Cauchy loss function (Section 2.4) leads to much more accurate estimates of the underlying profile parameters than a standard χ^2 metric.

4 PARAMETERS FROM INDIVIDUAL HALOES

The results presented so far have benefited from averaging the density profiles of numerous (at least 80) halos, which removes stochastic noise that arises from substructure, anisotropies such as filaments, and the finite number of particles in simulations. In this section, we ask whether the trends we found for averaged profiles can be extracted from the noisy distributions of individual fit parameters. On some level, the averaged profiles must reflect the individual profiles they are based on, but due to asymmetric scatter and the complex translation from profiles to best-fit parameters, the properties of mean/median profiles are not always the same as the mean/median properties of individual profiles.

As a result, fits (within the virial radius) are typically restricted

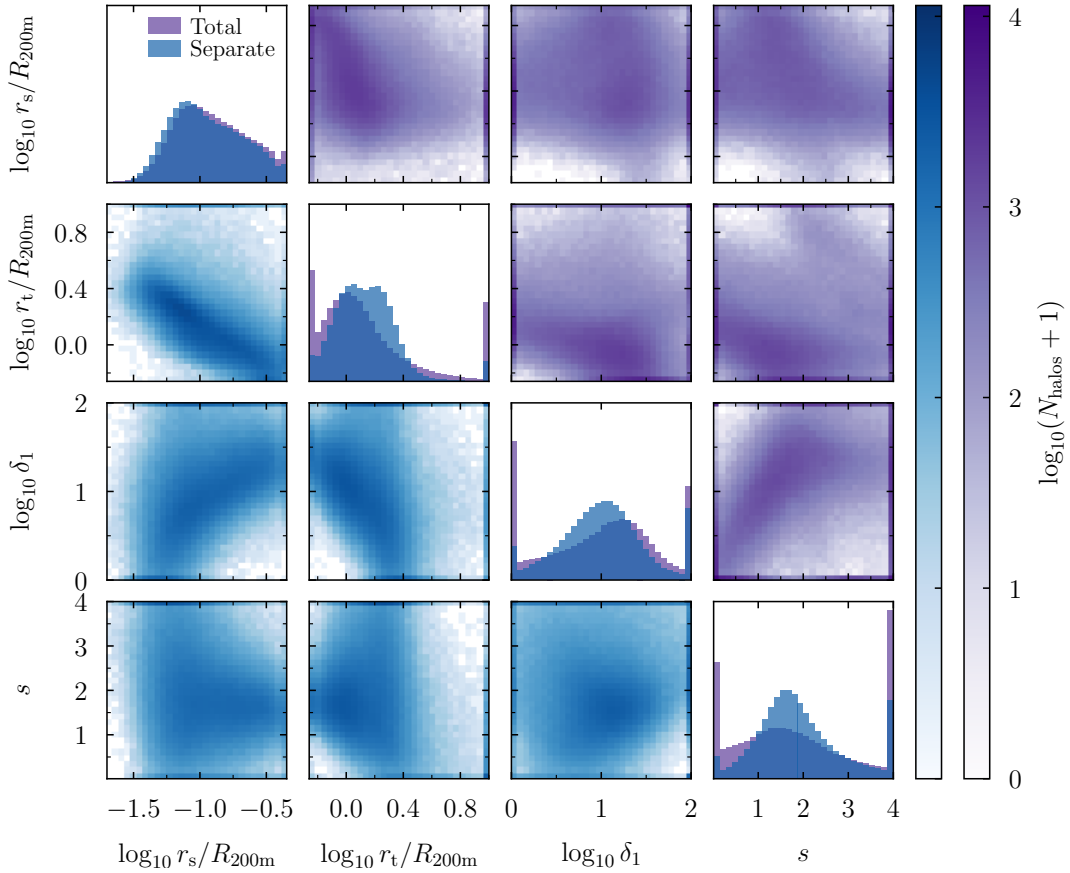


Figure 10. Parameter distributions (diagonal panels) and inter-relations (off-diagonal panels) of the best-fit parameters for individual profiles. Since α and β are fixed, we show only the scale and truncation radii as well as the normalization and slope of the infalling profile. As before, we omit the normalization ρ_s due to its trivial relationship with r_s . The bottom-left triangle (blue) shows the results from separate fits to orbiting and infalling profiles, which capture the ‘true’ shape of the underlying profiles (although there are caveats as discussed in the text). In the top-right triangle (purple), we compare to the less constrained, but more commonly available fits to the total profiles. The parameters fill most of the available space, showing that they are not strongly degenerate. The correlation between r_s and r_t is easily discernible in the separate fits (as in Figs. 3 and 4) but somewhat washed out in the total fits. A significant number of total profiles exhibit no clear truncation, meaning that r_t tends to its lowest or highest allowed values (purple histogram in second diagonal panel). Similarly, the parameters of the outer profile are less reliable in total fits because δ_1 and s develop a degeneracy that is not present in the separate fits.

to two free parameters, e.g., normalization and scale radius. Even adding a third parameter, such as Einasto’s α , leads to severe degeneracies (Udrescu et al. 2019). Thus, it is hopeless to fit our new model to individual profiles with all seven free parameters (five for the inner and two for the outer profile). Instead, we fix $\alpha = 0.18$ and $\beta = 3$, which leaves ρ_s , r_s , and r_t as the free parameters of the orbiting profile (Paper II). The chosen values for α and β provide a good fit to the vast majority of profiles. The preference for shallow profiles (low α) in fast-accreting halos (Fig. 6) is hard to discern in individual haloes.

We consider both separate fits to the orbiting and infalling profiles as well as total fits, where we fix δ_{\max} to its value from the orbiting-only fit but let ρ_s , r_s , r_t , δ_1 , and s vary. The separate fits tell us about the ‘true,’ underlying parameters of the orbiting and infalling components, whereas the total fits tell us what information persists in the sum of these terms. In most figures, we show the entire sample of about 378 000 fitted halo profiles (Paper II). The trends in sub-samples (such as Λ CDM at $z = 0$) tend to be slightly sharper but not fundamentally different (see online figures).

4.1 Parameter relations and degeneracies

Fig. 10 shows the relationships between fit parameters from individual halos, analogous to Fig. 3 but omitting the fixed α and β parameters. Whereas Fig. 3 showed results from the median and mean profiles in its lower and upper triangles, we now show parameters from the separate (blue) and total fits (purple). The diagonal panels compare the distributions of each parameter. Both r_s and r_t are shown in log space, and the range for r_s is slightly cut off at its lower end because only a negligible fraction of fits return $\log_{10} r_s/R_{200m} \lesssim -1.7$.

The parameters from the separate fits (blue) give us an impression of the true, underlying distribution of profile properties. The parameters fill a large fraction of the available parameter space, meaning that they are not degenerate. The r_s - r_t anti-correlation is still clearly observable in individual haloes, and the significant scatter reminds us that both scales contain separate information about the formation time and accretion rate of the haloes (see further discussion in Section 5.1). The other panels show weak correlations similar to those in the averaged profiles (Fig. 3): δ_1 correlates positively with r_s and negatively with r_t (indicating a connection with Γ that we discuss below), and s is more or less uncorrelated with the other parameters.

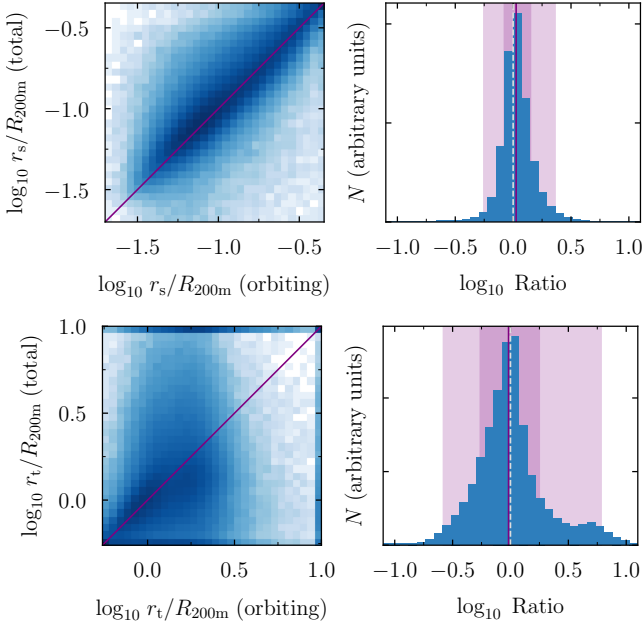


Figure 11. Recovery of r_s and r_t from fits to the total profile of individual halos, compared to fits to only the orbiting profile. The left panels show the density on a logarithmic scale similar to Fig. 10, whereas the right panels show histograms of the logarithmic ratio. Both r_s and r_t are recovered without bias but with significant 68% scatter of 0.15 dex in r_s and 0.25 dex in r_t .

4.2 Recovering parameters from the total profile

The distributions of the total fit results (purple panels in Fig. 10) clearly differ from the separate fits. For example, the r_s - r_t relation is weaker, the relations between the orbiting parameters and δ_1 have changed, and δ_1 and s are now visibly degenerate. These changes also manifest in the one-dimensional parameter distributions, which exhibit significant fractions of parameters in the lowest and highest allowed bins — a sign of poorly converged fits. These challenges are not surprising, given that we fit the profiles with five free parameters. While the infalling profile at $r \gg R_{200m}$ adds information, this part is also subject to large scatter (Paper I). For example, we observe some cases of density increasing with radius in the infalling part, which violates our requirement that $s \geq 0.01$ (Paper II). We conclude that it is difficult to extract reliable parameters for the infalling profile from individual halos.

The most interesting parameters, however, are r_s and r_t , which tell us about the structure of the orbiting term and the accretion history of the halo (Section 4.3). In Fig. 11, we directly investigate how well the total fits (y-axis) recover the values from the individual fits (x-axis). The right panels show histograms of the logarithm of the ratio between the two values. In both cases, the total estimates are essentially unbiased, but with 68% scatter of about 0.15 dex in r_s and 0.25 dex in r_t . From visual inspection of the fits, we find that large differences are typically due to unusually shaped profiles where our function (or any function) is a poor fit. In such cases, the fit sometimes determines a sensible r_s at the expense of an r_t that poorly represents the truncation, and vice versa.

In summary, individual profiles do contain information about both r_s and r_t , and thus about the formation time and recent accretion rate of halos. However, noise in the profiles means that the uncertainty on any individual parameter constraint is significant. These conclusions do not change if we consider sub-samples, such as WMAP7 at $z = 0$.

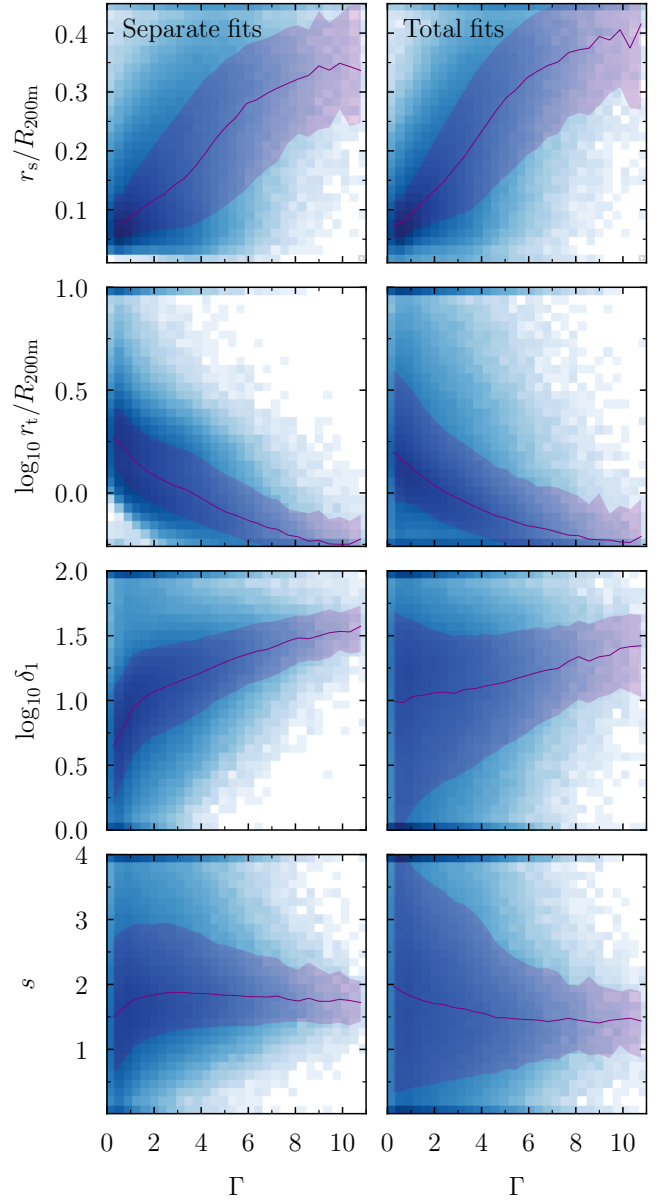


Figure 12. Relations between fit parameters and mass accretion rate for individual halos. The density of halos is shown as a logarithmic color map similar to Fig. 10. The purple lines and contours show the median and 68% interval. As in Fig. 10, we show results from fits to the separate orbiting and infalling profiles (left) and to the total profiles (right). As expected, the scatter is larger in the latter case for most parameters, especially for the normalization and slope of the outer profile. However, the median relations are remarkably stable to the fitting uncertainty introduced by fitting the total profiles. Most notably, the r_s - Γ relation is slightly tighter when fitting total profiles (see Section 4.2). The median r_t - Γ relation is virtually identical to that inferred from orbiting-only fits, demonstrating that it is, in principle, possible to retrieve accretion rates from individual profiles, albeit with large scatter.

4.3 Dependence on halo properties

In Section 3.2, we found that the accretion rate is a powerful predictor of the best-fit parameters. We now ask to what extent these relationships can be discerned in noisy individual profiles. Fig. 12 recreates Figs. 6 and 8, but now showing the distribution of individual fits (on roughly the same colour scale as Fig. 10) as well as its median and scatter (purple lines and shaded regions). We again

consider both separate fits (left column) and the more realistic case of total fits (right). The trends are similar to those of averaged profile parameters in Figs. 6 and 8: r_s increases with Γ because fast-accreting halos are young and have low concentration; r_t decreases with Γ ; the infalling profile is more prominent in fast-accreting halos (higher δ_1); and the slope s is more or less uncorrelated with Γ , in contrast to the averaged profiles. The latter observation indicates that the slight Γ - s correlation in Fig. 8 might be spurious in the sense that it arises from averaging over infalling profiles with different slopes.

Interestingly, the 68% scatter in the r_t - Γ relation is increased only mildly in the total fits (right column), indicating that a meaningful constraint on Γ could, in principle, be derived from individual halos. However, the rate of catastrophic outliers is much larger than for the separate fits. The r_s - Γ relation is tighter in the total fits, which is again explained by the fact that the separate fits are sometimes drawn to the correct r_t , at the expense of r_s (Section 4.2). We have also checked whether the ratio r_t/r_s (which one could understand as the ‘truncation concentration’) contains separate information from r_s/R_{200m} and r_t/R_{200m} . While this ratio can reach large values ($\gtrsim 20$ – 30) at low Γ , we find that it correlates less with Γ than r_t/R_{200m} , indicating that the conventionally defined concentration and r_t are cleaner ways to infer the overall and recent accretion histories (see also Shin & Diemer 2023).

Splitting the overall halo sample by redshift and/or cosmology makes the correlations in Fig. 12 slightly tighter but does not qualitatively alter them. The consistency between samples once again demonstrates that accretion history is the most important determinant of the parameters, with only minor influences from peak height and cosmology. We have checked that the relationships of the parameters with ν are similar to those of averaged profiles shown in Fig. 5, and that they mostly arise from the positive correlation between ν and Γ (see online figures).

5 DISCUSSION

We have analysed the best-fit parameters derived from fits to averaged and individual halo profiles, and established how they are connected to halo mass, accretion rate, redshift, and cosmology. In this section, we further discuss the connection to the overall accretion history (Section 5.1), how concentration differs between models (Section 5.2), and how the truncation radius is connected to other definitions of the halo boundary (Section 5.3).

5.1 The connection to a halo’s accretion history

Throughout this series of papers, we have alluded to the tight connection between a halo’s formation history and its density profile. In the ‘inside-out’ picture of halo formation, shells of dark matter accrete onto a halo seed, and the particle orbits remain at roughly the same (average) radii (e.g., Bertschinger 1985). Though simplified, this picture holds in principle, and halo profiles can be understood as a reflection of the critical density of the Universe at the times when shells were accreted (Ludlow et al. 2013; Correa et al. 2015; López-Cano et al. 2022). The time when a halo transitions from fast to slow accretion (which we shall identify with $a_{1/2}$, the scale factor when the halo had accreted half its current M_{200m}) imprints itself onto the profile as the scale radius (Wechsler et al. 2002; Zhao et al. 2009). In addition, DK14 showed that the entire profile is also sensitive to the recent accretion rate (over one halo crossing timescale; see also Xhakaj et al. 2022 and Shin & Diemer 2023). As this dependence

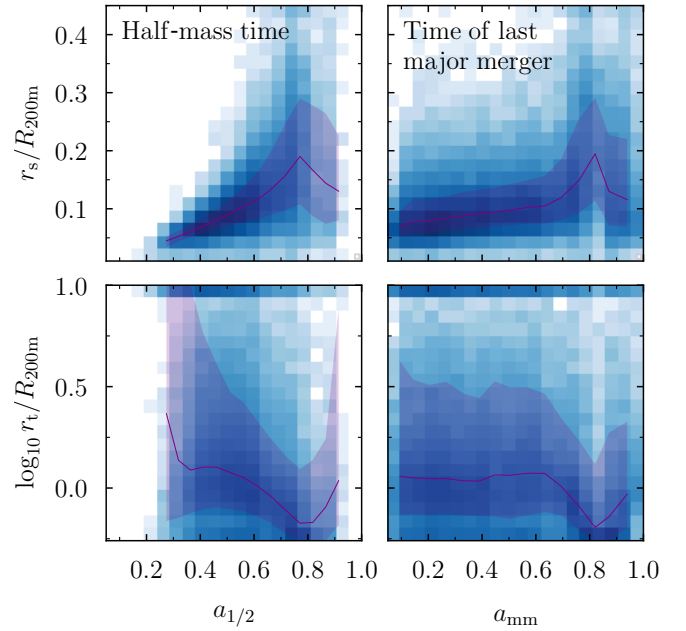


Figure 13. Relation of the characteristic radii r_s and r_t to the formation time ($a_{1/2}$, left) and the time of the last major merger (a_{mm} , right). The figure shows the WMAP7 sample at $z = 0$ only. We are using the fits to the total profile and thus not using any information from the separate orbiting profiles. We find the expected clear correlation between $a_{1/2}$ and r_s , whereas r_t only weakly correlates in the expected sense that later-forming halos accrete faster today. The time of the last major merger has a much smaller influence on the profiles, but it manifests as an increased r_s due to the merger dynamics and a dip in r_t due to the high accretion rate at $a = 0.8$, which corresponds to half a crossing time (the average time for the merging halo to reach pericentre).

is particularly relevant for r_t and the orbiting-infalling transition region, we have binned halos by Γ and charted the dependence of the profile parameters on this recent accretion rate. Binning by, say, concentration, would have aligned the profiles at smaller radii, around r_s . Given the strong correlation between $a_{1/2}$ and Γ , concentration-selected samples exhibit profiles similar to Γ -selected samples (Fig. 14 in DK14).

To verify this picture of the history-profile connection, we now consider two timescales in a halo’s history: the half-mass time $a_{1/2}$ and the time of the last major merger, a_{mm} (which CONSISTENT-TREES defines as a merger with mass ratio greater than 0.3, Behroozi et al. 2013). The latter allows us to test whether major mergers have a significant influence on the profiles, as recently suggested by the machine learning analysis of Lucie-Smith, Adhikari & Wechsler (2022). Instead of binning halo samples by $a_{1/2}$ and a_{mm} , Fig. 13 shows how r_s and r_t relate to $a_{1/2}$ and a_{mm} in individual profiles from the WMAP7 cosmology at $z = 0$. We use the more realistic fits to the total profile, which result in relatively reliable determinations of r_s and somewhat less reliable determinations of r_t . The relationship between the formation time and the scale radius is easily discernible in the top-left panel, where younger halos (high $a_{1/2}$) exhibit larger r_s/R_{200m} and thus smaller c_{200m} . While $a_{1/2}$ does correlate with r_t , it does so much more weakly, and in the expected way where later-forming halos have higher Γ and thus smaller r_t/R_{200m} .

The time of last merger, in contrast, correlates weakly with r_s and r_t except at very late times. Overall, we would expect that major mergers correlate with accretion in general, and that any long-term trend should thus go in the same direction as for $a_{1/2}$, which it does.

Interestingly, both r_s and r_t experience significant fluctuations for $a_{\text{mm}} \approx 0.8$, which corresponds exactly to the time it takes particles and subhalos to cross $R_{200\text{m}}$ (half a halo crossing time, or 2.7 Gyr at $z = 0$). We thus understand the peak in r_s to be caused by the disturbance of the halo due to the major merger (Wang et al. 2020b) and the dip in r_t to correspond to the high mass accretion rate caused by the merger. For mergers that happened even more recently, the response has not yet had time to propagate to the apocenters of recently added particles, and thus to r_t . The parameters of the outer profile are not shown in Fig. 13 because they do not strongly correlate with $a_{1/2}$ and a_{mm} . Presumably, they would be informed by the future, not past, accretion rate of halos.

These findings are highly compatible with Lucie-Smith, Adhikari & Wechsler (2022), whose machine learning algorithm identifies three features in the accretion history that strongly influence the final density profile: the formation time, recent accretion, and last major merger. The question then arises whether those three timescales should be associated with three free parameters in the density profile, i.e., whether there is a parameter beyond r_s and r_t that is sensitive to major mergers. Indeed, Lucie-Smith et al. (2022) find that they need three ‘basis functions’ to describe the profiles inside of $2 R_{200\text{m}}$, which matches the three free parameters in our orbiting fit (when α and β are fixed). However, it is not clear that any one basis function, or any free parameter, is clearly associated with major mergers. Given the large scatter in the relations in Fig. 13, the effects of mergers are probably too diverse and short-lived to be easily identified in the characteristic shapes of profiles, even though a machine learning tool can statistically detect them.

We have established the history-profile connection on a halo-by-halo level, but cosmological analyses give broadly compatible results. For example, Sánchez et al. (2022) show that the non-linear power spectra (which contain information from the infalling profiles around halos) can be accurately modelled as a function of the variance and the linear growth factor and its derivatives. This success highlights that the growth factor encodes the majority of the cosmological information probed by mildly non-linear scales. In Paper I, we interpreted the infalling profile on those scales to depend on ν (analogous to the variance σ) and n_{eff} .

5.2 On the meaning of concentration in different profile models

As we have discussed at length, $r_s/R_{200\text{m}} = 1/c_{200\text{m}}$ is a key property of density profiles that couples tightly to a halo’s formation history. Its value, however, depends somewhat sensitively on the profile form used (NFW vs. Einasto vs. our new model) and on the fitting methodology (maximum radius, loss function, and so on). For example, NFW and Einasto concentrations differ by up to 15% (e.g., Dutton & Macciò 2014). We thus caution that the scale radii derived from our fits to total individual profiles are not directly analogous to those in other works. For example, ROCKSTAR fits (out to the virial radius) result in r_s being more than 50% higher than our NFW fits on average, presumably because we fit the NFW profile out to radii that it was not designed to describe. Einasto fits (with fixed α) broadly agree with fits of the new model, though with significant scatter. As expected, Models A and B agree almost exactly, except for very low concentrations where the difference in slope at r_s (which can move slightly away from -2 in Model A) makes a difference.

Given these ambiguities, it makes more sense to compare the concentrations of averaged profiles. Here, we do not detect significant differences between the Model B fits to the orbiting and total profiles, indicating that the scale radius is reliably determined by the profiles. Comparing to NFW and Einasto concentrations, we find

that the new model measures up to 20% lower r_s (higher c) at low peak height and up to 20% higher r_s (lower c) at high peak height, though with some scatter in the individual datasets (see online figures). This comparison refers to NFW and Einasto fits to the total profile, i.e., with an infalling term, but out to arbitrary radii.

In summary, concentration depends moderately on the fitting function for averaged profiles, and strongly for individual profiles. We defer more detailed calibrations to future work.

5.3 How are the truncation and splashback radii related?

In recent years, numerous works have proposed definitions of the halo boundary that are intended to be more physically motivated than spherical overdensity radii. These suggestions have included the ‘static mass’ in shells with negative mean radial velocity (Cuesta et al. 2008), the splashback radius R_{sp} (DK14, Adhikari, Dalal & Chamberlain 2014), the ‘edge radius’ where only infalling subhalos contribute to the satellite population (Tomooka et al. 2020; Aug et al. 2021, 2023), the ‘truncation radius’ at the minimum of $r^2\rho$ that optimizes the halo model (García et al. 2021, 2023, not to be confused with our r_t ; see also Pizzardo, Diaferio & Rines 2024), and the ‘depletion radius’ where the bias profile reaches its minimum (Fong & Han 2021). Moreover, the splashback radius has been approximated as r_{steep} , the radius where the logarithmic slope of the total density profile is steepest (More, Diemer & Kravtsov 2015), as percentiles of the apocentre distribution of particles on their first orbit (Diemer 2017), and as non-spherical shells determined by local density caustics (Mansfield, Kravtsov & Diemer 2017).

Fundamentally, most of these definitions try to capture the same underlying physical feature: the phase-space boundary beyond which material cannot orbit. In perfect spherical symmetry, all definitions would give the same answer because the largest apocenter radius coincides with an infinitely sharp caustic in density (Fillmore & Goldreich 1984; Bertschinger 1985; Shi 2016). In practice, all definitions encounter various difficulties: the density caustic is smoothed out and highly non-spherical, making it hard to identify in individual halo profiles and even in some stacked samples; the location of r_{steep} is a trade-off between the orbiting and infalling profiles; there is no one ‘edge’ radius to which satellites can orbit, only higher and higher percentiles of the apocentre distribution; and this distribution is, at any given time, affected by the complex collapse of a halo’s particles and mergers.

The best-fit truncation radius in our profile model represents yet another measurable quantity that relates to properties of the underlying halo, such as its mass and accretion rate. In this section, we thus quantify the relationship between r_t , r_{steep} , and the dynamically determined R_{sp} as measured by SPARTA.

5.3.1 Truncation vs. steepest slope

In Fig. 14, we test whether r_t or the commonly used r_{steep} is more tightly connected to accretion rate. Both are determined from fits to the total profile, as they would be observationally. The top panel of Fig. 14 demonstrates that the Γ - r_t relation is tight at all accretion rates/Compared to Fig. 6 we have left out the self-similar Universes, which exhibit somewhat larger scatter. For the plotted Λ CDM cosmologies at $z = 0$, we find

$$r_t/R_{200\text{m}} \approx 0.49 + 1.29 e^{-\Gamma/1.61}. \quad (9)$$

The dotted line in Fig. 14 shows the relation proposed by DK14, where we have approximately converted Γ to the DK14 definition of

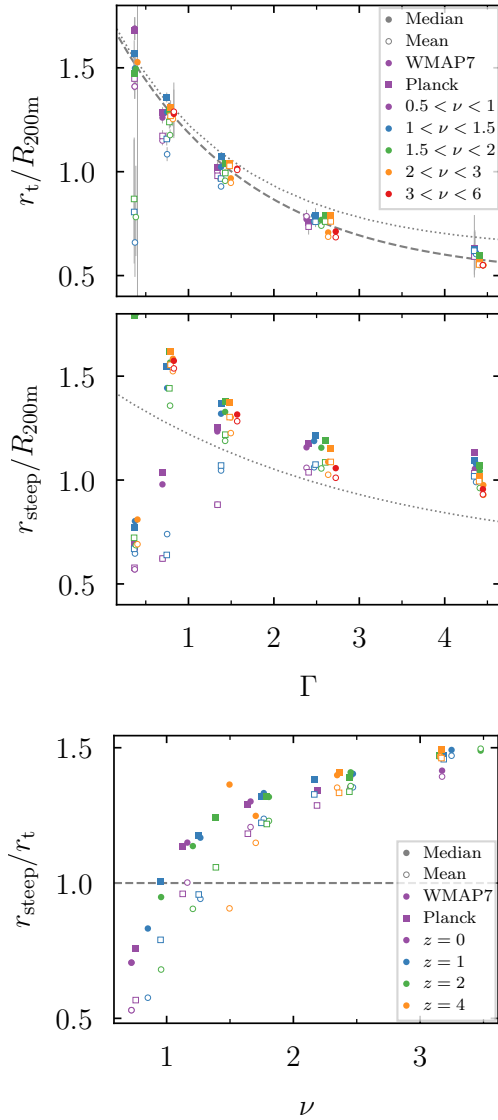


Figure 14. Relation between r_t and r_{steep} , the radius where the logarithmic slope of the fitted profile is steepest. The top two panels demonstrate that r_t has a cleaner relationship to the accretion rate than r_{steep} , especially at low Γ where r_{steep} is increasingly determined by the infalling profile. The dotted and dashed lines in the top panel show the relation suggested by DK14 and equation 9, respectively. The slight disagreement arises due to the different meaning of r_t in the two functions. The dotted line in the middle panel shows the relation suggested by More, Diemer & Kravtsov 2015. Here the disagreement with our new fits arises because of the slightly different r_{steep} preferred by the DK14 and new fitting functions, and because the relation was not calibrated to match the lowest ν and Γ bins. The bottom panel shows that a well-defined trend in r_{steep}/r_t arises not only as a function of Γ (top panels) but also as a function of ν .

accretion rate (Diemer 2020). The approximate match means that the DK14 and new fitting functions assign roughly the same meaning to r_t , but this is only true for Γ -selected profiles in DK14, not for their ν -selected profiles (Section 3.2.3). The new function has the advantage that it can fit both types of samples with similar values of β , and thus more or less the same meaning of r_t .

In contrast to r_t , the $r_{\text{steep}}-\Gamma$ relation breaks down at $\Gamma \lesssim 2$ (middle panel of Fig. 14). The reasons are two-fold: at low Γ , the edge of the orbiting term moves outwards, where it competes with a higher

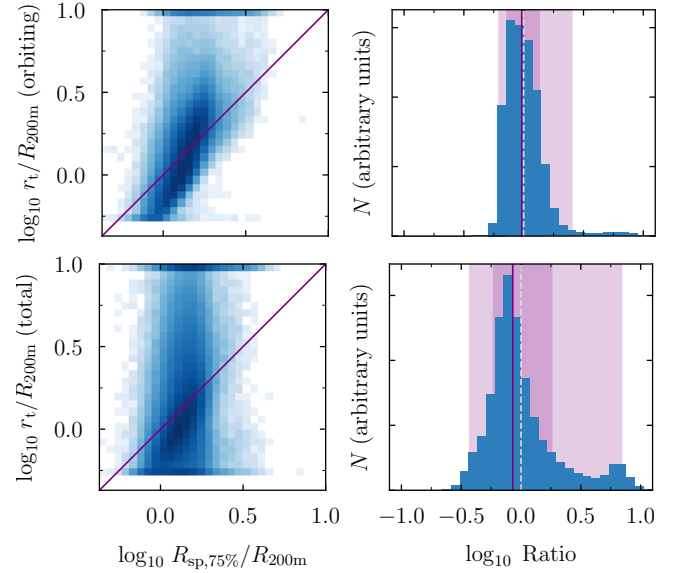


Figure 15. Recovery of the splashback radius from r_t as measured in fits to the separate orbiting profile (top) and the total profile (bottom). The panels have the same meaning as in Fig. 11. Here, the SPARTA algorithm has measured the splashback radius for each halo dynamically, defining it as the 75th percentile of the apocentres of particles on their first orbit. We have made no cuts on the sample, meaning that not all splashback radii are reliable. The underlying r_t of the orbiting profile tracks the splashback radius closely, although the relationship is not exactly linear (with a 68% scatter of 0.13 dex). The more realistic r_t measured in total fits exhibits much larger scatter of 0.24 dex, confirming that it is difficult to infer R_{sp} from individual halo profiles.

density of infalling material; and the second caustic due to particles on their second orbit, which resides at smaller radii, can become the location of r_{steep} (e.g., Wang, Wang & Mo 2022). We conclude that r_t is the more stable indicator of accretion rate, and that one should use the best-fit r_t rather than trying to determine r_{steep} . The bottom panel of Fig. 14 highlights that the ratio r_{steep}/r_t falls on a well-defined, redshift-independent sequence with ν , but the two radii can differ by up to 50%.

Another difficulty with r_{steep} is that its inferred value depends on the fitting function, or on the algorithm used to compute the slope (O’Neil et al. 2021). This issue is illustrated by the dotted gray line in the middle panel of Fig. 14, which shows the fitting function of More, Diemer & Kravtsov (2015). This relation does not match the r_{steep} computed from our new fits because r_{steep} from DK14 fits is about 10% lower at high Γ and vice versa (see online figures). We find that the DK14 function is slightly better than our new model at capturing the r_{steep} of the actual average profiles, but the point is that r_{steep} is an inherently model-dependent, fickle quantity that should not be used when inferring halo properties.

5.3.2 Truncation vs. splashback

Part of the draw of measuring r_{steep} is that it is a stand-in for the splashback radius, but the relationship between r_{steep} and the dynamical definition of R_{sp} is complex (Diemer 2020). We might as well ask how accurately r_t can approximate R_{sp} in individual halos. As discussed in Section 4.2, fits to only the orbiting term give a much more accurate estimate of r_t , but this success cannot be replicated in observations. Fig. 15 thus compares both values to $R_{\text{sp},75\%}$ as measured by SPARTA (that is, the radius that encloses 75% of the first-orbit

apocentres, see Diemer 2017). We find similar results for other percentile definitions, although their overall normalization shifts. Similar to Fig. 11, we plot both 2D histograms of the variables and 1D histograms of their logarithmic ratio, using the entire halo sample.

As expected, the orbiting-only r_t and R_{sp} are strongly correlated, although not exactly along the 1:1 relation. Thus, r_t could be used as a proxy for R_{sp} , but both measurements demand the dynamical analysis of particle orbits (either the apocentre or pericentre counters in SPARTA). When deriving r_t from the entire profile, the scatter gets much larger (bottom panels of Fig. 15). While there is still a clear correlation for the majority of haloes, there are also extreme outliers where r_t simply cannot be measured. This result is not surprising, given that the inability to measure R_{sp} from individual profiles was the motivation for algorithms such as SPARTA in the first place.

In summary, precise measurements of the splashback radius are difficult, regardless of whether it is defined as r_{steep} in averaged profiles or dynamically in individual halos. However, by inferring r_t , we can directly connect the profile fits to the accretion rate and other halo properties. We defer a comparison of r_t to boundary definitions other than the splashback radius because they are either non-trivial to compute (e.g., García et al. 2021; Aung et al. 2021) or rely on the relationship between averaged profiles and the linear matter-matter correlation function, ξ_{mm} (Fong & Han 2021). As already shown in DK14, we find that the infalling profiles are not well described by a bias times ξ_{mm} prescription, meaning that it will be difficult to physically connect the meaning of r_t to estimates such as the minimum in the bias profile.

6 CONCLUSIONS

We have investigated the parameter space of the truncated exponential plus power-law fitting function for halo density profiles proposed in Paper II. We have considered both averaged and individual halo profiles, as well as fits to the total profile and its separate orbiting and infalling components. Our main conclusions are as follows.

- (i) The best-fit parameters span a well-defined space where r_t/R_{200m} and β describe the location and sharpness of the truncation of the orbiting term. The parameters exhibit only modest degeneracies, but some of them do fall on well-defined sequences that are mostly determined by accretion rate.
- (ii) The two characteristic scale and truncation radii, r_s and r_t , reflect the formation time and recent accretion rate of halos, respectively. They are correlated because young halos tend to accrete faster today, but they capture separate information. Both r_s and r_t can be accurately inferred from stacked, total profiles.
- (iii) The relationship between α and peak height is an artefact of fitting truncated profiles with the Einasto form. When using the new fitting function, α is independent of ν and decreases with Γ .
- (iv) The best-fit parameters for individual halo profiles (with $\alpha = 0.18$ and $\beta = 3$) are naturally much noisier than those based on averaged profiles, but they broadly exhibit the same inter-relations and capture the same information about the accretion rate.
- (v) The best-fit truncation radii of averaged profiles are tightly connected to Γ , more tightly so than the radius where the slope is steepest. Similar inferences can be made even from individual profiles, though with significant scatter.

The key test of these conclusions will be to fit the new model to observational data using MCMC chains, both with and without some of the priors suggested by our results (such as the preferred values for α and β). Another important application of this work will be to

build a full forward model of halo density profiles, where the profile parameters are predicted from halo properties such as their accretion history.

ACKNOWLEDGEMENTS

I am grateful to Susmita Adhikari, Rafael García, Edgar Salazar, Luisa Lucie-Smith, and Eduardo Rozo for productive conversations. I thank Phil Mansfield for sharing the color scheme used in several figures. This research was supported in part by the National Science Foundation under Grant numbers 2206690 and 2338388. The computations were run on the MIDWAY computing cluster provided by the University of Chicago Research Computing Center and on the DeepThought2 cluster at the University of Maryland. This research extensively used the python packages NUMPY (Harris et al. 2020), SCIPY (Virtanen et al. 2020), MATPLOTLIB (Hunter 2007), and COLOSUS (Diemer 2018).

DATA AVAILABILITY

The SPARTA code that was used to extract the dynamically split density profiles from our simulations is publicly available in a BitBucket repository, bitbucket.org/bdiemer/sparta. An extensive online documentation can be found at bdiemer.bitbucket.io/sparta. The SPARTA output files (one file per simulation) are available in an hdf5 format at erebos.astro.umd.edu/erebos/sparta. A Python module to read these files is included in the SPARTA code. Additional figures are provided online on the author's website at benediktdiemer.com/data. The full particle data for the Erebus N -body simulations are too large to be permanently hosted online, but they are available upon request.

REFERENCES

- Adhikari S., Dalal N., Chamberlain R. T., 2014, JCAP, 11, 19
- Anbajagane D., Evrard A. E., Farahi A., 2022, MNRAS, 509, 3441
- Auger M. W., Budzynski J. M., Belokurov V., Koposov S. E., McCarthy I. G., 2013, MNRAS, 436, 503
- Aung H., Nagai D., Rozo E., García R., 2021, MNRAS, 502, 1041
- Aung H., Nagai D., Rozo E., Wolfe B., Adhikari S., 2023, MNRAS, 521, 3981
- Baltz E. A., Marshall P., Oguri M., 2009, J. Cosmology Astropart. Phys., 1, 15
- Baxter E. et al., 2017, ApJ, 841, 18
- Behroozi P. S., Wechsler R. H., Wu H.-Y., 2013, ApJ, 762, 109
- Behroozi P. S., Wechsler R. H., Wu H.-Y., Busha M. T., Klypin A. A., Primack J. R., 2013, ApJ, 763, 18
- Bertschinger E., 1985, ApJS, 58, 39
- Brown S. T., McCarthy I. G., Diemer B., Font A. S., Stafford S. G., Pfiefer S., 2020, MNRAS, 495, 4994
- Brown S. T., McCarthy I. G., Stafford S. G., Font A. S., 2022, MNRAS, 509, 5685
- Bullock J. S., Kolatt T. S., Sigad Y., Somerville R. S., Kravtsov A. V., Klypin A. A., Primack J. R., Dekel A., 2001, MNRAS, 321, 559
- Burkert A., 1995, ApJ, 447, L25
- Chang C. et al., 2018, ApJ, 864, 83
- Correa C. A., Wyithe J. S. B., Schaye J., Duffy A. R., 2015, MNRAS, 450, 1521
- Crocce M., Pueblas S., Scoccimarro R., 2006, MNRAS, 373, 369
- Cuesta A. J., Prada F., Klypin A., Moles M., 2008, MNRAS, 389, 385
- De Boni C., Serra A. L., Diaferio A., Giocoli C., Baldi M., 2016, ApJ, 818, 188
- Dehnen W., 1993, MNRAS, 265, 250

- Diemand J., Kuhlen M., 2008, *ApJ*, 680, L25
- Diemer B., 2017, *ApJS*, 231, 5
- Diemer B., 2018, *The Astrophysical Journal Supplement Series*, 239, 35
- Diemer B., 2020, *ApJS*, 251, 17
- Diemer B., 2022, *MNRAS*, 513, 573
- Diemer B., 2023, *MNRAS*, 519, 3292
- Diemer B., Joyce M., 2019, *ApJ*, 871, 168
- Diemer B., Kravtsov A. V., 2014, *ApJ*, 789, 1
- Diemer B., Kravtsov A. V., 2015, *ApJ*, 799, 108
- Dutton A. A., Macciò A. V., 2014, *MNRAS*, 441, 3359
- Eckert D., Ettori S., Robertson A., Massey R., Pointecouteau E., Harvey D., McCarthy I. G., 2022, *A&A*, 666, A41
- Einasto J., 1965, *Trudy Astrofizicheskogo Instituta Alma-Ata*, 5, 87
- Einasto J., 1969, *Astrophysics*, 5, 67
- Enomoto Y., Nishimichi T., Taruya A., 2024, *MNRAS*, 527, 7523
- Ettori S., Gastaldello F., Leccardi A., Molendi S., Rossetti M., Buote D., Meneghetti M., 2010, *A&A*, 524, A68
- Farahi A., Evrard A. E., McCarthy I., Barnes D. J., Kay S. T., 2018, *MNRAS*, 478, 2618
- Fillmore J. A., Goldreich P., 1984, *ApJ*, 281, 1
- Fong M., Han J., 2021, *MNRAS*, 503, 4250
- Gao L., Navarro J. F., Cole S., Frenk C. S., White S. D. M., Springel V., Jenkins A., Neto A. F., 2008, *MNRAS*, 387, 536
- García R., Rozo E., Becker M. R., More S., 2021, *MNRAS*, 505, 1195
- García R., Salazar E., Rozo E., Adhikari S., Aung H., Diemer B., Nagai D., Wolfe B., 2023, *MNRAS*, 521, 2464
- Gunn J. E., Gott, III J. R., 1972, *ApJ*, 176, 1
- Harris C. R. et al., 2020, *Nature*, 585, 357
- Hayashi E., White S. D. M., 2008, *MNRAS*, 388, 2
- Hernquist L., 1990, *ApJ*, 356, 359
- Hunter J. D., 2007, *Computing in Science Engineering*, 9, 90
- Jaffe W., 1983, *MNRAS*, 202, 995
- Klypin A., Yepes G., Gottlöber S., Prada F., Heß S., 2016, *MNRAS*, 457, 4340
- Klypin A. A., Trujillo-Gomez S., Primack J., 2011, *ApJ*, 740, 102
- Knollmann S. R., Power C., Knebe A., 2008, *MNRAS*, 385, 545
- Komatsu E. et al., 2011, *ApJS*, 192, 18
- Lewis A., Challinor A., Lasenby A., 2000, *ApJ*, 538, 473
- López-Cano D., Angulo R. E., Ludlow A. D., Zennaro M., Contreras S., Chaves-Montero J., Aricò G., 2022, *MNRAS*, 517, 2000
- Lucie-Smith L., Adhikari S., Wechsler R. H., 2022, *MNRAS*, 515, 2164
- Lucie-Smith L., Peiris H. V., Pontzen A., 2024, *Phys. Rev. Lett.*, 132, 031001
- Lucie-Smith L., Peiris H. V., Pontzen A., Nord B., Thiyaalingam J., Piras D., 2022, *Phys. Rev. D*, 105, 103533
- Ludlow A. D., Angulo R. E., 2017, *MNRAS*, 465, L84
- Ludlow A. D. et al., 2013, *MNRAS*, 432, 1103
- Ludlow A. D., Schaye J., Bower R., 2019, *MNRAS*, 488, 3663
- Mansfield P., Avestruz C., 2021, *MNRAS*, 500, 3309
- Mansfield P., Kravtsov A. V., Diemer B., 2017, *ApJ*, 841, 34
- Merritt D., Graham A. W., Moore B., Diemand J., Terzić B., 2006, *AJ*, 132, 2685
- More S., Diemer B., Kravtsov A. V., 2015, *ApJ*, 810, 36
- More S. et al., 2016, *ApJ*, 825, 39
- Muni C., Pontzen A., Sanders J. L., Rey M. P., Read J. I., Agertz O., 2024, *MNRAS*, 527, 9250
- Navarro J. F., Frenk C. S., White S. D. M., 1995, *MNRAS*, 275, 720
- Navarro J. F., Frenk C. S., White S. D. M., 1996, *ApJ*, 462, 563
- Navarro J. F., Frenk C. S., White S. D. M., 1997, *ApJ*, 490, 493
- Navarro J. F. et al., 2010, *MNRAS*, 402, 21
- Nipoti C., 2015, *ApJ*, 805, L16
- Oguri M., Bayliss M. B., Dahle H., Sharon K., Gladders M. D., Natarajan P., Hennawi J. F., Koester B. P., 2012, *MNRAS*, 420, 3213
- O’Neil S., Barnes D. J., Vogelsberger M., Diemer B., 2021, *MNRAS*, 504, 4649
- Pizzardo M., Diaferio A., Rines K. J., 2024, *A&A*, 682, A80
- Planck Collaboration et al., 2014, *A&A*, 571, A16
- Prada F., Klypin A. A., Cuesta A. J., Betancort-Rijo J. E., Primack J., 2012, *MNRAS*, 423, 3018
- Salazar E. M., Rozo E., García R., Kokron N., Adhikari S., Diemer B., Osinga C., 2024, *arXiv e-prints*, arXiv:2406.04054
- Sánchez A. G., Ruiz A. N., Jara J. G., Padilla N. D., 2022, *MNRAS*, 514, 5673
- Shi X., 2016, *MNRAS*, 459, 3711
- Shin T. et al., 2019, *MNRAS*, 487, 2900
- Shin T. et al., 2021, *MNRAS*, 507, 5758
- Shin T.-h., Diemer B., 2023, *MNRAS*, 521, 5570
- Springel V., 2005, *MNRAS*, 364, 1105
- Sugiura H., Nishimichi T., Rasera Y., Taruya A., 2020, *MNRAS*, 493, 2765
- Tasitsiomi A., Kravtsov A. V., Gottlöber S., Klypin A. A., 2004, *ApJ*, 607, 125
- Tomooka P., Rozo E., Wagoner E. L., Aung H., Nagai D., Safonova S., 2020, *MNRAS*, 499, 1291
- Udrescu S. M., Dutton A. A., Macciò A. V., Buck T., 2019, *MNRAS*, 482, 5259
- Umetsu K., 2020, *A&ARv*, 28, 7
- Umetsu K., Diemer B., 2017, *ApJ*, 836, 231
- Virtanen P. et al., 2020, *Nature Methods*, 17, 261
- Wang J., Bose S., Frenk C. S., Gao L., Jenkins A., Springel V., White S. D. M., 2020a, *Nature*, 585, 39
- Wang K., Mao Y.-Y., Zentner A. R., Lange J. U., van den Bosch F. C., Wechsler R. H., 2020b, *MNRAS*, 498, 4450
- Wang X., Wang H., Mo H. J., 2022, *A&A*, 667, A99
- Wechsler R. H., Bullock J. S., Primack J. R., Kravtsov A. V., Dekel A., 2002, *ApJ*, 568, 52
- Wiesner M. P. et al., 2012, *ApJ*, 761, 1
- Khakaj E., Leauthaud A., Lange J., Hearin A., Diemer B., Dalal N., 2022, *MNRAS*, 514, 2876
- Zhao D. H., Jing Y. P., Mo H. J., Börner G., 2009, *ApJ*, 707, 354
- Zhou Y., Han J., 2024, *arXiv e-prints*, arXiv:2407.08381

This paper has been typeset from a \LaTeX file prepared by the author.